

The *TESS*-Keck Survey II: Masses of Three Sub-Neptunes Transiting the Galactic Thick-Disk Star TOI-561

LAUREN M. WEISS,¹ FEI DAI,² DANIEL HUBER,¹ JOHN M. BREWER,³ KAREN A. COLLINS,⁴ DAVID R. CIARDI,⁵ ELISABETH C. MATTHEWS,⁶ CARL ZIEGLER,⁷ STEVE B. HOWELL,⁸ NATALIE M. BATALHA,⁹ IAN J. M. CROSSFIELD,¹⁰ COURTNEY DRESSING,¹¹ BENJAMIN FULTON,¹² ANDREW W. HOWARD,¹³ HOWARD ISAACSON,^{14,15} STEPHEN R. KANE,¹⁶ ERIK A. PETIGURA,¹⁷ PAUL ROBERTSON,¹⁸ ARPITA ROY,¹³ RYAN A. RUBENZAHN,^{13,*} ZACHARY R. CLAYTOR,¹ KEIVAN G. STASSUN,¹⁹ ASHLEY CHONTOS,^{1,*} STEVEN GIACALONE,²⁰ PAUL A. DALBA,^{16,†} TEO MOCNIK,²¹ MICHELLE L. HILL,¹⁶ COREY BEARD,¹⁸ JOSEPH M. AKANA MURPHY,^{22,*} LEE J. ROSENTHAL,¹³ AIDA BEHMARD,^{23,*} JUDAH VAN ZANDT,¹⁷ JACK LUBIN,¹⁸ MOLLY R. KOSIAREK,^{22,24} MICHAEL B. LUND,²⁵ JESSIE L. CHRISTIANSEN,²⁵ RACHEL A. MATSON,²⁶ CHARLES A. BEICHMAN,⁵ JOSHUA E. SCHLIEDER,²⁷ ERICA J. GONZALES,^{28,29} CÉSAR BRICEÑO,³⁰ NICHOLAS LAW,³¹ ANDREW W. MANN,³¹ KEVIN I. COLLINS,³² PHIL EVANS,³³ AKIHIKO FUKUI,^{34,35} ERIC L. N. JENSEN,³⁶ FELIPE MURGAS,^{37,38} NORIO NARITA,^{39,40,41,42} ENRIC PALLE,^{37,38} HANNU PARVIAINEN,^{37,38} RICHARD P. SCHWARZ,⁴³ THIAM-GUAN TAN,⁴⁴ JON JENKINS,⁸ GEORGE RICKER,⁴⁵ SARA SEAGER,^{46,47,48} JOSHUA N. WINN,⁴⁹

¹*Institute for Astronomy, University of Hawai'i, 2680 Woodlawn Drive, Honolulu, HI 96822, USA*

²*Division of Geological and Planetary Sciences, 1200 E California Blvd, Pasadena, CA, 91125, USA*

³*Department of Physics and Astronomy, San Francisco State University, 1600 Holloway Ave, San Francisco, CA 94132, USA*

⁴*Center for Astrophysics | Harvard & Smithsonian, 60 Garden Street, Cambridge, MA 02138, USA*

⁵*NASA Exoplanet Science Institute, Caltech/IPAC, Pasadena, CA 91125*

⁶*Observatoire de l'Université de Genève, 51 Chemin des Maillettes, 1290 Versoix, Switzerland*

⁷*Dunlap Institute for Astronomy and Astrophysics, University of Toronto, 50 St. George Street, Toronto, Ontario M5S 3H4, Canada*

⁸*NASA Ames Research Center, Moffett Field, CA 94035, USA*

⁹*Department of Astronomy and Astrophysics, University of California, Santa Cruz, CA 95060, USA*

¹⁰*Department of Physics & Astronomy, University of Kansas, 1082 Malott, 1251 Wescoe Hall Dr., Lawrence, KS 66045, USA*

¹¹*501 Campbell Hall, University of California at Berkeley, Berkeley, CA 94720, USA*

¹²*NASA Exoplanet Science Institute/Caltech-IPAC, MC 314-6, 1200 E California Blvd, Pasadena, CA 91125, USA*

¹³*Department of Astronomy, California Institute of Technology, Pasadena, CA 91125, USA*

¹⁴*Department of Astronomy, University of California Berkeley, Berkeley CA 94720, USA*

¹⁵*Centre for Astrophysics, University of Southern Queensland, Toowoomba, QLD, Australia*

¹⁶*Department of Earth and Planetary Sciences, University of California, Riverside, CA 92521, USA*

¹⁷*Department of Physics & Astronomy, University of California Los Angeles, Los Angeles, CA 90095, USA*

¹⁸*Department of Physics & Astronomy, University of California Irvine, Irvine, CA 92697, USA*

¹⁹*Vanderbilt University, Department of Physics & Astronomy, 6301 Stevenson Center Ln., Nashville, TN 37235, USA*

²⁰*Department of Astronomy, University of California Berkeley, Berkeley, CA 94720, USA*

²¹*Gemini Observatory, Northern Operations Center, 670 N. A'ohoku Place, Hilo, HI 96720, USA*

²²*Department of Astronomy and Astrophysics, University of California, Santa Cruz, CA 95064, USA*

²³*Division of Geological and Planetary Science, California Institute of Technology, Pasadena, CA 91125, USA*

²⁴*NSF Graduate Research Fellow*

²⁵*NASA Exoplanet Science Institute, Caltech/IPAC, Pasadena, CA 91125, USA*

²⁶*US Naval Observatory, 3450 Massachusetts Ave. NW., Washington, DC 20392, USA*

²⁷*Exoplanets and Stellar Astrophysics Laboratory, Mail Code 667, NASA Goddard Space Flight Center, Greenbelt, MD 20771, USA*

²⁸*University of California, Santa Cruz, 1156 High St., Santa Cruz, CA, 95064, USA*

²⁹*National Science Foundation Graduate Research Fellow*

³⁰*CCerro Tololo Inter-American Observatory, Casilla 603, La Serena 1700000, Chile*

³¹*Department of Physics and Astronomy, The University of North Carolina at Chapel Hill, Chapel Hill, NC 27599-3255, USA*

³²*George Mason University, 4400 University Drive, Fairfax, VA, 22030 USA*

³³*El Sauce Observatory, Coquimbo Province, Chile*

³⁴*Department of Earth and Planetary Science, Graduate School of Science, The University of Tokyo, 7-3-1 Hongo, Bunkyo-ku, Tokyo 113-0033, Japan*

³⁵*Instituto de Astrofísica de Canarias, Vía Láctea s/n, E-38205 La Laguna, Tenerife, Spain*

³⁶*Dept. of Physics & Astronomy, Swarthmore College, Swarthmore PA 19081, USA*

³⁷*Instituto de Astrofísica de Canarias (IAC), 38205 La Laguna, Tenerife, Spain*

³⁸*Departamento de Astrofísica, Universidad de La Laguna (ULL), 38206, La Laguna, Tenerife, Spain*

³⁹*Komaba Institute for Science, The University of Tokyo, 3-8-1 Komaba, Meguro, Tokyo 153-8902, Japan*

⁴⁰*JST, PRESTO, 3-8-1 Komaba, Meguro, Tokyo 153-8902, Japan*

⁴¹*Astrobiology Center, 2-21-1 Osawa, Mitaka, Tokyo 181-8588, Japan*

⁴²*Instituto de Astrofísica de Canarias (IAC), 38205 La Laguna, Tenerife, Spain*

⁴³*Patashnick Voorheesville Observatory, Voorheesville, NY 12186, USA*

⁴⁴*Perth Exoplanet Survey Telescope, Perth, Western Australia*

⁴⁵*Kavli Institute for Astrophysics and Space Research, Massachusetts Institute of Technology, Cambridge, MA 02139, USA*

⁴⁶*Department of Physics and Kavli Institute for Astrophysics and Space Research, Massachusetts Institute of Technology, Cambridge, MA 02139, USA*

⁴⁷*Department of Earth, Atmospheric and Planetary Sciences, Massachusetts Institute of Technology, Cambridge, MA 02139, USA*

⁴⁸*Department of Aeronautics and Astronautics, MIT, 77 Massachusetts Avenue, Cambridge, MA 02139, USA*

⁴⁹*Department of Astrophysical Sciences, Princeton University, 4 Ivy Lane, Princeton, NJ 08544, USA*

ABSTRACT

We report the discovery of TOI-561, a multiplanet system containing an ultra-short period planet (USP), based on photometry from the NASA *TESS* Mission and ground-based follow-up. This bright ($V = 10.2$) star hosts three small transiting planets: TOI-561 b (TOI-561.02, $P=0.44$ days, $R_p=1.45 \pm 0.11 R_\oplus$), c (TOI-561.01, $P=10.8$ days, $R_p = 2.90 \pm 0.13 R_\oplus$), and d (TOI-561.03, $P=16.4$ days, $R_p=2.32 \pm 0.16 R_\oplus$). The star is chemically ($[\text{Fe}/\text{H}] = -0.41 \pm 0.05$, $[\alpha/\text{Fe}] = +0.23 \pm 0.05$) and kinematically consistent with the galactic thick disk population, making TOI-561 one of the oldest (10 ± 3 Gyr) and most metal-poor planetary systems discovered yet. We confirm the planetary nature of the candidates with high-contrast imaging, ground-based photometric follow-up and radial velocities from Keck/HIRES. Planet b has a mass and density of $3.2 \pm 0.8 M_\oplus$ and $5.6_{-1.7}^{+2.2} \text{ g cm}^{-3}$, consistent with a rocky composition. Its lower-than-average density is consistent with an iron-poor composition, although an Earth-like iron-to-silicates ratio is not ruled out. Planet c is $6.5 \pm 2.4 M_\oplus$ and $1.45 \pm 0.55 \text{ g cm}^{-3}$, and planet d is $2.4_{-1.7}^{+2.3} M_\oplus$ and $1.1_{-0.7}^{+1.1} \text{ g cm}^{-3}$, both of which are consistent with an interior rocky core overlaid with a low-mass volatile envelope. TOI-561 b is the first rocky world around a galactic thick-disk star confirmed with radial velocities and one of the best rocky planets for thermal emission studies.

Keywords: planetary systems, exoplanets, TESS

1. INTRODUCTION

The NASA *Kepler* Mission demonstrated that small planets are abundant in the Milky Way Galaxy (Borucki et al. 2010; Howard et al. 2012; Fressin et al. 2013; Petigura et al. 2013). What are the properties of small planets around nearby, bright stars, including their bulk and atmospheric compositions? How do planet properties vary with stellar type and age? The NASA *TESS* mission is a two-year, all-sky survey that is finding small, transiting planets around nearby F,G,K, and M type stars (Ricker et al. 2015). The all-sky strategy enables TESS to sample the transiting planets around brighter stars spanning a wider range of properties than were represented in the pencil-beam *Kepler* Survey.

A *TESS* Mission level-one science goal is to measure the masses of 50 sub-Neptune sized transiting planets¹.

The *TESS*-Keck Survey (TKS) is a multi-institutional collaboration of Keck-HIRES users who are pooling Keck-HIRES time to meet this science goal and others (see TKS-I, Dalba et al. 2020, and also TKS-0, Chontos et al. in prep.). The TKS science goals include determining the masses, bulk densities, orbits, and host star properties of planets in our survey. Our survey targets were selected to answer broad questions about planet properties, formation, and evolution.

TESS Object of Interest (TOI) 561 is a $V = 10.2$ star that advances three of the TKS science goals: (1) to compare planetary siblings in systems with multiple transiting planets, (2) to characterize ultra-short period planets (USPs), and (3) to study planetary systems across a variety of stellar types. Systems with multiple transiting planets provide excellent natural laboratories for testing the physics of planet formation, since the planets all formed around the same star and from the same protoplanetary disk. TOI-561 is a bright star for which planet masses, interior compositions, and eventually atmospheric compositions can be determined

* NSF Graduate Research Fellow

† NSF Astronomy and Astrophysics Postdoctoral Fellow

¹ NASA TESS Mission, accessed 2020 Aug 23

through follow-up efforts. Our investigation of TOI-561 advances our goal to compare the fundamental physical properties of small-planet siblings in extra-solar systems.

TOI-561 also hosts a USP that has an orbital period of < 1 day and a radius consistent with a rocky composition (e.g., Weiss & Marcy 2014; Rogers 2015)². The present-day location of USPs corresponds to the former evacuated region of the protoplanetary disk. Because the protoplanetary disk cavity forms during the first few million years of the star’s existence, this inner region should have been depleted of the building blocks necessary to assemble planets. Thus, the formation of USPs is poorly understood, but likely involves migration to overcome the low local density of solids. Characterizing the mass and bulk density of TOI-561 b clarify how it and other USPs formed.

We did not initially select TOI-561 for its host star properties, but we discovered during our investigation that TOI-561 is a member of the galactic thick disk. Its low metallicity, high alpha abundance, and old age make it a special case that may advance our understanding of both multiplanet systems and the formation of USPs. Its unusual chemistry, kinematics, and age also address a third goal of TKS, which is to study planetary systems across a variety of stellar types.

In §2, we describe the TESS photometry, including the signals of the three transiting planet candidates. In §3 we characterize the host star. We describe our methods of planet candidate validation with ground-based photometry (§4) and high-resolution imaging (§5), and confirmation with radial velocities (§6). We describe the planet masses and densities in §7. We discuss the planetary system orbital dynamics and prospects for future atmospheric characterization in §8. We conclude in §9.

2. TESS PHOTOMETRY

The vetting team of the TESS Science Processing Operations Center (SPOC) identified three transiting planets in their analysis of the photometry for TESS Input Catalog (TIC) ID 377064495 (Jenkins et al. 2016; Twicken et al. 2018; Li et al. 2019). The pre-search data conditioned simple aperture photometry (PDCSAP) is shown in Figure 1 (Stumpe et al. 2014; Smith et al. 2012; Stumpe et al. 2012). The star was observed in Sector 8. The SPOC-defined aperture is overlaid on the target in a Full Frame Image (FFI) in Figure 2. The first planet candidate the SPOC pipeline detected is at $P = 10.78$ days (TOI-561.01, planet c) based on two transits, with SNR 9.8. After masking the flux near the transits of

planet c, the SPOC pipeline detected a planet candidate at $P = 0.45$ days (TOI-561.02, planet b) based on 55 transits, with SNR 10.0. After masking the flux near transits of both planets c and b, the SPOC pipeline detected a planet candidate at $P = 16.4$ days (TOI-561.03, planet d), which transits twice, with SNR 9.2.

There is a gap partway through the time series that complicates the interpretation of the transit signals. The timing of the gap corresponds to a data download and also an unplanned interruption in communication between the instrument and spacecraft³. The USP transited 55 times during the *TESS* observations, leading to a robust ephemeris determination (although individual transits are too shallow to identify by eye in the photometry; see §4 for the phase-folded photometry and §6 for the RV planet confirmation). However, only two transits of planet c and two transits of planet d were detected. The transits of c and d occurred on different sides of the data gap. For planet c, the non-detection of additional transits in the *TESS* photometry leads to a robust determination of the orbital period at 10.78 days, but for planet d, two orbital periods are allowed: either at 16.37 days (there is no transit during the gap), or at 8.19 days (there is a transit in the gap, see the dotted blue arrow in Figure 1).

The three planetary signatures passed all of the data validation diagnostic tests except for the difference image centroiding test, which placed the source for 561 b within $11''$, 561 c within $23''$, and 561 d within $7''$ (and a passing score for this test). They all passed the ghost diagnostic test as well, indicating that if they were due to background eclipsing binaries, the offending star would have to be within a pixel of the location of the target star. All three planet candidates pass the SPOC pipeline odd-even test, with insignificant differences between the depths of odd-numbered vs. even-numbered transits.

Through ground-based photometry, we refined the orbital ephemerides of the planet candidates (although the aliasing of planet d’s orbit was not resolved) and validated their planetary natures. The acquisition of ground-based photometry and our best-fit model to the transit data (including both *TESS* and ground-based photometry) are described in §4.

3. STELLAR PROPERTIES

3.1. High-Resolution Spectroscopy

We obtained a high signal-to-noise spectrum of TOI-561 to determine atmospheric parameters and detailed chemical abundances using the line list and forward

² The definition of USPs as having $P < 1$ day is somewhat arbitrary; see Sanchis-Ojeda et al. (2014) vs. Dai et al. (2018).)

³ TESS Data Release Notes: Sector 8, DR10

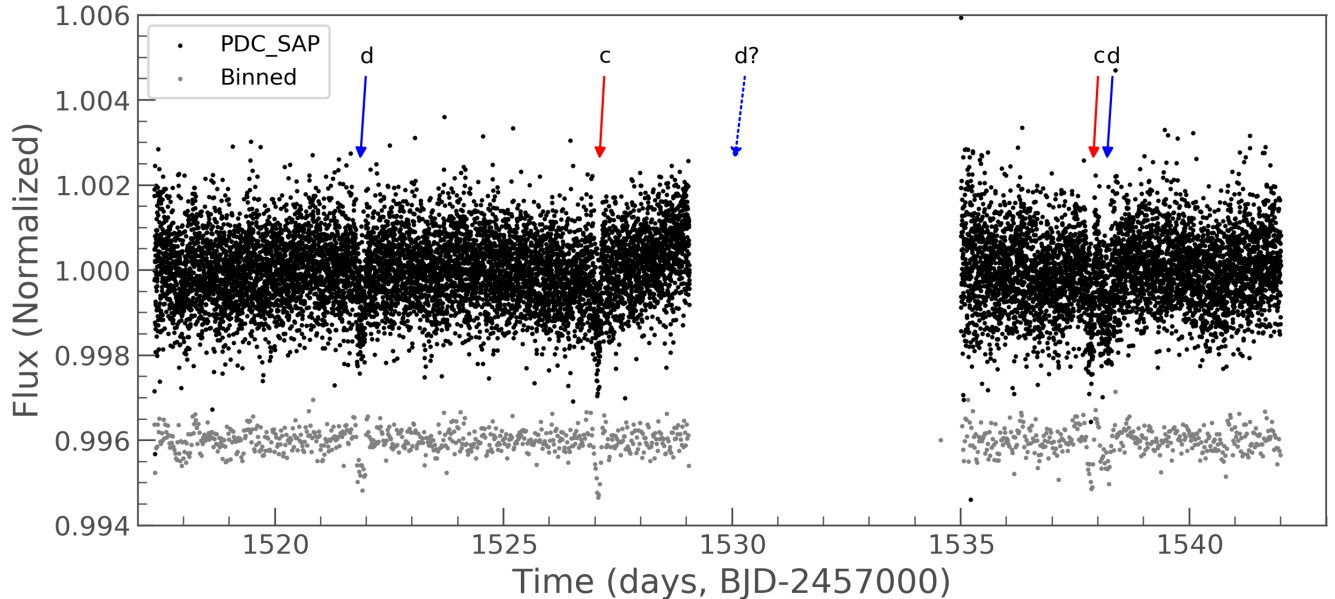


Figure 1. The pre-search data conditioned SAP *TESS* photometry of TOI-561 (black points) and the same photometry but binned every 13 data points and flattened (gray points, with flux offset). Individual transits of planets c (red arrows) and d (blue arrows) are marked. A third transit of planet d could have occurred in the time series gap (blue dotted arrow). A planet at $P = 0.44$ days (planet b) is also present, but the transits are too shallow to see in these data (see Figures 4 and 6).

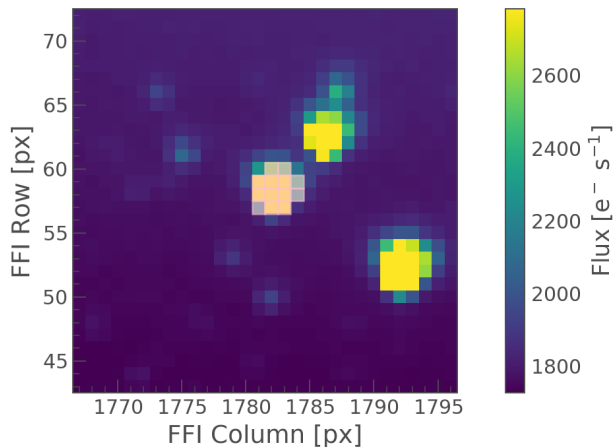


Figure 2. The *TESS* Full-Frame Image centered on TOI-561. The SPOC-defined aperture is a pale pink overlay on the central star. The *TESS* plate scale is $21''$ per pixel. The target star has *TESS* magnitude 9.49. False positive scenarios in which the bright nearby stars are eclipsing binaries are ruled out with follow-up ground based photometry (see §4).

modeling procedure of Brewer et al. (2016). The modeling uses Spectroscopy Made Easy (SME) (Valenti & Piskunov 1996; Piskunov & Valenti 2017) in an iterative scheme that alternates between solving for global stellar properties and a detailed abundance pattern. We begin by estimating T_{eff} from B-V colors then fitting for T_{eff} , $\log g$, $[M/H]$, Doppler line broadening, and the abundances of the α elements calcium, silicon, and titanium.

All other elements are scaled solar values based on the overall metallicity given by $[M/H]$ and the initial abundances are set to solar. The temperature of the resulting model is perturbed by ± 100 K and used as input to re-fit the spectrum. The χ^2 weighted average of the global stellar parameters are then fixed and used as the input for the next step of fitting for the abundances of 15 elements. Simultaneous fitting of the elements is critical in obtaining precise abundances due to chemical processes in the stellar photosphere (Ting et al. 2018).

The global parameters and abundance pattern obtained in the first iteration are then used as an initial guess for a second fitting following the same steps. Finally, the macroturbulence is set using a T_{eff} relation from Brewer et al. (2016) and we solve for the projected rotational velocity, $v \sin i$, with all other parameters fixed. The resulting gravities have been shown to be consistent with those from asteroseismology to within 0.05 dex and the abundance uncertainties are between 0.01 - 0.04 dex (Brewer et al. 2015). An empirical correction is applied to the abundances as a function of temperature (Brewer et al. 2016), which adds additional uncertainty to the absolute abundance, especially at temperatures between 5000 K - 5500 K, and we adopt 0.05 dex uncertainty for most elements. Our analysis yielded a low stellar metallicity and high alpha-abundance ($[Fe/H] = -0.41 \pm 0.05$, $[\alpha/Fe] = +0.23 \pm 0.05$, see Table 1).

The effective temperature derived from the SME analysis (5326 ± 25 K)⁴ is in good agreement with alternative estimates using Specmatch-Synth (5249 ± 110 K, [Petrigura 2015](#)), Specmatch-Emp (5302 ± 110 K, [Yee et al. 2017](#)), color- T_{eff} relations applied in the *TESS* Input Catalog (5440 ± 110 K, [Stassun et al. 2018](#)) and applying a $J-K$ color- T_{eff} relation (5300 ± 110 K, [Casagrande et al. 2010](#)). We adopted the SME-derived solution, with an error bar calculated from the standard deviation of T_{eff} estimates from different methods: 5326 ± 64 K.

For each spectrum, we measure the Mt. Wilson S-value, an indicator of the chromospheric magnetic activity. The Mt. Wilson S-value is a measure of the strength of the emission cores in the Ca II H and K lines relative to nearby continuum flux. Our procedure for determining the S-values is described in [Isaacson & Fischer \(2010\)](#). See §6, Table 3, for the full S-value time series. A Lomb-Scargle periodogram of the S-values results in peaks near 100 days and 230 days, neither of which is near the expected rotation period or magnetic activity cycle of this old K dwarf.

3.2. Distance Modulus & Isochrone Modeling

Stellar atmosphere and interior models are typically calculated using a solar-scaled α element abundance mixture and thus assume $[\text{Fe}/\text{H}] = [\text{M}/\text{H}]$. To account for the non-solar α abundances of TOI-561, we averaged the individual abundance measurements for $[\text{Mg}/\text{H}]$, $[\text{Si}/\text{H}]$, $[\text{Ca}/\text{H}]$ and $[\text{Ti}/\text{H}]$ to derive $[\alpha/\text{Fe}] = +0.23 \pm 0.05$, and then applied the calibration by [Salaris et al. \(1993\)](#) to convert the measured $[\text{Fe}/\text{H}]$ value into an overall metal abundance, yielding $[\text{M}/\text{H}] = -0.24 \pm 0.10$:

$$[\text{M}/\text{H}] = [\text{Fe}/\text{H}] + \log_{10}(0.694 \times 10^{[\alpha/\text{Fe}]} + 0.306). \quad (1)$$

We adopted a conservative uncertainty of 0.1 dex for $[\text{M}/\text{H}]$ to account for potential systematics in the [Salaris et al. \(1993\)](#) calibration.

Next, we used T_{eff} , $[\text{M}/\text{H}]$, $\log g$, the *Gaia* DR2 parallax (adjusted for the 0.082 ± 0.033 mas zero-point offset for nearby stars reported by [Stassun & Torres 2018](#)), 2MASS K-band magnitude, a 3D dust map and bolometric corrections to calculate a luminosity by solving the standard distance modulus, as implemented in the “direct mode” of *isoclassify* ([Huber et al. 2017](#)). We then combined the derived luminosity with T_{eff} and $[\text{M}/\text{H}]$ to infer additional stellar parameters (mass, radius, density) using the “grid mode” of *isoclassify*, which performs probabilistic inference of stellar parameters using a grid of MIST isochrones ([Choi et al. 2016](#)).

The isochrone-derived $\log g$ (4.50 ± 0.03 dex) is in excellent agreement with spectroscopy (4.52 ± 0.05 dex), confirming that no additional iteration in the above steps is required for a self-consistent solution. The derived age of the isochrone fit is 10 ± 3 Gyr, consistent with the mean age of a galactic thick disc star (see following section).

The full set of stellar parameters are listed in Table 1. The results show that TOI-561 is an early-K dwarf with a radius of $R_{\star} = 0.832 \pm 0.019 R_{\odot}$ and mass $M_{\star} = 0.805 \pm 0.030 M_{\odot}$. We note that the quoted uncertainties are formal error bars and do not include potential systematic errors due to the use of different model grids ([Tayar et al. in prep.](#)). For example, the stellar radius in Table 1 is 3% lower than predicted from an application of the Stefan-Boltzmann law using either the “direct mode” of *isoclassify* or SED fitting ([Stassun et al. 2017](#)), both of which yield $0.86 \pm 0.02 R_{\odot}$. However, this 3% ($\approx 1\sigma$) difference does not significantly affect our main conclusions on the properties of the planets in the TOI-561 system, since the planet density errors are dominated by uncertainties in the planet masses (see §7).

We used the stellar evolution model fitting tool *kiauhoku* ([Claytor et al. 2020](#)) to estimate the rotation period of TOI-561. Using the stellar T_{eff} , $[\text{Fe}/\text{H}]$, and $[\alpha/\text{Fe}]$ from Table 1 as inputs, and assuming an age of 10 ± 3 Gyr, we found two different model-dependent estimates of the rotation period. Assuming the magnetic braking law described in [van Saders & Pinsonneault \(2013\)](#), we found $P_{\text{rot}} = 38.5 \pm 7.3$ days, but assuming the stalled-braking law of [van Saders et al. \(2016\)](#), we found $P_{\text{rot}} = 35.7 \pm 3.4$ days. These rotation periods are consistent with the upper limit of $v \sin i$ we determined spectroscopically. However, the estimated rotation periods differ significantly from the periodicity identified in the Mt. Wilson S-value activity indices (see Table 3), suggesting that the rotation period is not detected in the S-value time series. A rotation period of > 30 days is likely too long to identify in the single sector of TESS photometry.

3.3. Galactic Evolution

Early studies of star counts in the Milky Way revealed two distinct populations in the galactic disk which dominate at different scale heights, commonly denoted the “thin” and “thick” disk population ([Gilmore & Reid 1983](#)). Spectroscopic and photometric surveys have shown that these populations can be approximately separated based on kinematics and chemical abundances, with thick disk stars being kinematically hotter (e.g. [Fuhrmann 1998](#)), older ([Bensby et al. 2005](#)), more metal-

⁴ This error is the formal uncertainty, not the adopted error.

Table 1. Host Star Characteristics

Basic Properties	
Tycho ID	243-1528-1
TIC ID	377064495
Gaia DR2 ID	3850421005290172416
Right Ascension	19 37 25.575
Declination	+38 56 50.515
Tycho V_T Magnitude	10.25
<i>TESS</i> Magnitude	9.49
2MASS K Magnitude	8.39
<i>Gaia</i> DR2 Astrometry	
Parallax, π (mas)	11.627 ± 0.067
Radial Velocity (km/s)	79.54 ± 0.56
Proper Motion in RA (mas/yr)	-108.432 ± 0.088
Proper Motion in DEC (mas/yr)	-61.511 ± 0.094
High-Resolution Spectroscopy	
Effective Temperature, T_{eff} (K)	5326 ± 64
Surface Gravity, $\log g$ (cm s^{-2})	4.52 ± 0.05
Projected rotation speed, $v \sin i$ (km s^{-1})	< 2.0
$\log R'_{\text{HK}}$ (dex)	-5.1
Iron Abundance, [Fe/H] (dex)	-0.41 ± 0.05
Carbon Abundance, [C/H] (dex)	-0.19 ± 0.05
Nitrogen Abundance, [N/H] (dex)	-0.51 ± 0.05
Oxygen Abundance, [O/H] (dex)	$+0.09 \pm 0.05$
Sodium Abundance, [Na/H] (dex)	-0.39 ± 0.05
Magnesium Abundance, [Mg/H] (dex)	-0.20 ± 0.05
Aluminum Abundance, [Al/H] (dex)	-0.19 ± 0.05
Silicon Abundance, [Si/H] (dex)	-0.24 ± 0.05
Calcium Abundance, [Ca/H] (dex)	-0.27 ± 0.05
Titanium Abundance, [Ti/H] (dex)	-0.20 ± 0.05
Vanadium Abundance, [V/H] (dex)	-0.27 ± 0.05
Chromium Abundance, [Cr/H] (dex)	-0.43 ± 0.05
Manganese Abundance, [Mn/H] (dex)	-0.60 ± 0.05
Nickel Abundance, [Ni/H] (dex)	-0.37 ± 0.05
Yttrium Abundance, [Y/H] (dex)	-0.42 ± 0.05
Alpha Abundance, [α /Fe] (dex)	$+0.23 \pm 0.05$
Distance Modulus & Isochrone Modeling	
Stellar Luminosity, L_\star (L_\odot)	0.522 ± 0.017
Stellar Mass, M_\star (M_\odot)	0.805 ± 0.030
Stellar Radius, R_\star (R_\odot)	0.832 ± 0.019
Stellar Density, ρ_\star (ρ_\odot)	1.38 ± 0.11
Surface Gravity, $\log g$ (cgs)	4.500 ± 0.030
Age (Gyr)	10 ± 3

Notes: The *TESS* magnitude is adopted from the *TESS* Input Catalog (Stassun et al. 2018), and the kinematics are taken from Gaia DR2 (Lindegren et al. 2018). Stellar parameters from isochrone modeling are formal uncertainties only, and do not incorporate systematic errors from different model grids.

poor and enriched in α process elements (e.g. Fuhrmann 1998).

The formation of the thick disk is still debated, with scenarios including external processes such as the accretion of stars from the disruption of a satellite galaxy (e.g. Abadi et al. 2003) and induced star formation from mergers with other galaxies (e.g. Brook et al. 2004), or a natural dynamical evolution of our galaxy including radial migration (Schönrich & Binney 2009a,b). While the mere existence of a distinct thick disk is still in question (Bovy et al. 2012), spectroscopic and asteroseismic surveys have confirmed that chemically-identified “thick disk” stars belong to the old population of our galaxy, with typical ages of ~ 11 Gyr (Silva Aguirre et al. 2018).

The detection of exoplanets around different galactic stellar populations can provide powerful insights into their formation and evolution (Adibekyan et al. 2012). For example, the discovery of five sub-Earth sized planets orbiting the thick-disk star Kepler-444 (Campante et al. 2015) demonstrated for the first time that terrestrial planet formation has occurred for at least ~ 11 Gyr, and the discovery of a close M dwarf companion demonstrated that this process can even proceed in a truncated protoplanetary disk (Dupuy et al. 2016). While *TESS* probes nearby stellar populations it has significant potential to expand this sample. Indeed, Gan et al. (2020) recently presented the first *TESS* exoplanet orbiting a thick disk star identified based on kinematics.

Figure 3 compares the chemical properties of TOI-561 with a sample of field stars in the *TESS* candidate target list (CTL) observed by the GALAH survey (De Silva et al. 2015; Sharma et al. 2018) and a sample of known exoplanet hosts from the Hypatia catalog (Hinkel et al. 2014). We calculated [α /Fe] for stars in the Hypatia catalog in the same manner as for TOI-561 and discarded stars with abundance uncertainties > 0.2 dex (calculated from the scatter between different methods). TOI-561 is consistent with the thick disk in terms of its chemical abundances, in agreement with the high proper motions measured by Gaia (Table 1) and the kinematic classification of TOI-561 by Carrillo et al. (2020). To independently confirm the kinematic classification, we used the *UVW* velocity vector of TOI-561 via the online velocity calculator of Rodriguez (2016), finding $(U, V, W) = (-60.0, -70.9, +16.7)$ km s^{-1} . Using the probabilistic framework of Bensby et al. (2004) and Bensby et al. (2014) we find a thick-to-thin disk probability ratio of $TD/D = 19$, indicating strong evidence that this star is a member of the thick disk.

TOI-561 is the first chemically and kinematically confirmed thick-disk exoplanetary system discovered by *TESS*, the fifth known thick disk star known to host mul-

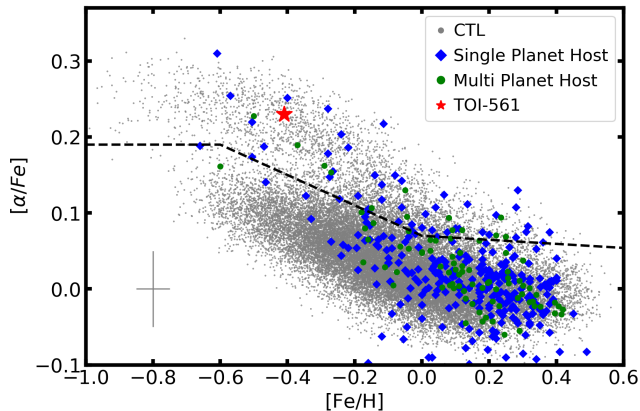


Figure 3. Iron abundance versus $[\alpha/\text{Fe}]$ for stars in the *TESS* candidate target list (CTL) observed by the GALAH survey (De Silva et al. 2015; Sharma et al. 2018) and a sample of exoplanet host stars taken from Hypatia catalog (Hinkel et al. 2014). Known exoplanet hosts are separated into those with a single known planet (blue diamonds) and multiple known planets (green circles). The position of TOI-561 is marked by a red star. The black dashed line approximately separates the galactic thin disk and thick disk populations

multiple planets, and the first thick-disk star known to host an ultra-period short planet. This further demonstrates that (1) small, rocky planets can form in metal-poor environments (consistent with Buchhave et al. 2012), (2) USPs are not tidally destroyed around old stars (consistent with Hamer & Schlaufman 2020), and (3) rocky planets have been forming for nearly the age of the universe.

4. TIME-SERIES PHOTOMETRIC FOLLOW-UP AND ANALYSIS

We acquired ground-based time-series follow-up photometry of TOI-561 as part of the *TESS* Follow-up Observing Program (TFOP)⁵ to attempt to (1) rule out nearby eclipsing binaries (NEBs) as potential sources of the *TESS* detections and (2) detect the transits on target to refine the *TESS* ephemerides. We used the **TESS Transit Finder**, which is a customized version of the **Tapir** software package (Jensen 2013), to schedule our transit observations.

4.1. LCOGT

We observed TOI-561 using the Las Cumbres Observatory Global Telescope (LCOGT) 1-m networks (Brown et al. 2013) in Pan-STARRS z -short (z_s) band. The telescopes are equipped with 4096×4096 SINISTRO cameras having an image scale of $0''.389 \text{ pixel}^{-1}$ resulting

in a $26' \times 26'$ field of view. The images were calibrated using the standard LCOGT BANZAI pipeline (McCully et al. 2018), and the photometric data were extracted using the **AstroImageJ** (AIJ) software package (Collins et al. 2017). A full transit window of TOI-561 b was observed continuously for 205 minutes on 19 April 2019 UT from the LCOGT Siding Spring Observatory (SSO) node. TOI-561 c was observed continuously for 381 minutes on 03 February 2020 UT from the LCOGT McDonald Observatory node and again on 17 March 2020 UT from the LCOGT Cerro Tololo Inter-American Observatory (CTIO) node for 230 minutes and then later on the same epoch from the LCOGT SSO node for 269 minutes. TOI-561 d was observed continuously for 300 minutes on 24 April 2020 UT from the LCOGT SSO node.

4.2. MuSCAT2

We observed full transit windows of TOI-561 b continuously for 120 minutes on 23 April 2019 UT and 24 May 2020 UT simultaneously in g , r , i , and z_s bands with the MuSCAT2 multi-color imager (Narita et al. 2019) installed at the 1.52 m Telescopio Carlos Sanchez (TCS) in the Teide Observatory, Spain. The photometry was carried out using standard aperture photometry calibration and reduction steps with a dedicated MuSCAT2 photometry pipeline, as described in Parviainen et al. (2020).

4.3. PEST

We observed a full transit window of TOI-561 b continuously for 205 minutes on 22 April 2019 UT in R_c band from the Perth Exoplanet Survey Telescope (PEST) near Perth, Australia. The 0.3 m telescope is equipped with a 1530×1020 SBIG ST-8XME camera with an image scale of $1''.2 \text{ pixel}^{-1}$ resulting in a $31' \times 21'$ field of view. A custom pipeline based on **C-Munipack**⁶ was used to calibrate the images and extract the differential photometry.

4.4. El Sauce

We observed a full transit window of TOI-561 b continuously for 206 minutes on 23 April 2019 UT in R_c band from El Sauce Observatory in Coquimbo Province, Chile. The 0.36 m Evans telescope is equipped with a 1536×1024 SBIG STT-1603-3 camera with an image scale of $1''.47 \text{ pixel}^{-1}$ resulting in a $18.8' \times 12.5'$ field of view. The photometric data were extracted using AIJ.

4.5. TOI-561 b

⁵ TFOP website

⁶ <http://c-munipack.sourceforge.net>

The TOI-561 b SPOC pipeline transit depth is generally too shallow (290 ppm) for ground-based detection, so we checked all three stars within $2.5'$ that are bright enough to have caused the SPOC detection (i.e. *TESS* magnitude < 18.1) for a possible NEB that could be contaminating the SPOC photometric aperture. Using a combination of the LCOGT, MuSCAT2, PEST, and El Sauce TOI-561 b follow-up observations, we rule out the possibility of a contaminating NEB at the SPOC pipeline ephemeris.

4.6. TOI-561 c

In the LCOGT observation of TOI-561 c on 03 February 2020 UT, we detected a 142 min early (0.3σ) ~ 1100 ppm egress, relative to the nominal SPOC ephemeris, in a $9''.7$ radius aperture around the target star, which is not contaminated with any known Gaia DR2 stars. As a result, we revised the follow-up orbital period to 10.778325 days. The 17 March 2020 UT LCOGT CTIO and SSO observations then detected an on-time ingress and egress, respectively, at the revised ephemeris.

4.7. TOI-561 d

The LCOGT observation of TOI-561 d on 24 April 2020 UT covered an egress ± 150 minutes (approximately 0.5σ) relative to the nominal SPOC pipeline ephemeris. The data rule out a 923 ppm egress, as well as possible NEBs within $2.5'$, during the limited time coverage of the SPOC ephemeris uncertainty.

4.8. Transit Modeling

Here we perform a joint analysis of *TESS* light curve and ground-based follow-up to refine the planetary parameters. We downloaded the *TESS* light curve from the Mikulski Archive for Space Telescopes (MAST, Figure 1). We isolated the transits of each planet with a window of three times the transit duration. We removed long term stellar variability/instrumental effect by fitting a cubic spline to the light curve after removing the transits. We also downloaded the ground-based follow-up observation from the [ExoFOP website](#). We used the **BATMAN** (Kreidberg) package for transit modeling, using the transit ephemerides reported by the *TESS* team as an initial guess for our model. Our model uses the mean stellar density ρ_* as a global parameter on all three planets. For each planet, we allowed the radius ratio R_p/R_* , the impact parameter b , the orbital period P , and the mid-transit time T_c to vary freely. We assumed circular orbits for all three planets. The mean stellar density ρ_* and the orbital period P together constrain the scaled semi-major axes a/R_* of each planet. We adopted a

Table 2. Transit Parameters

Parameter	Median $\pm 1\sigma$
Stellar Density ρ_* (ρ_\odot)	1.10 ± 0.10
Limb Darkening q_1	$0.2_{-0.2}^{+0.2}$
Limb Darkening q_2	$0.4_{-0.2}^{+0.3}$
Planet b	
Orbital Period P_b (days)	$0.446590_{-0.000021}^{+0.000014}$
Mid-Transit Time T_c (BJD)	$2458517.4988_{-0.0030}^{+0.0022}$
Radius Ratio R_p/R_*	$0.01602_{-0.0011}^{+0.0010}$
Impact Parameter b	0.3 ± 0.2
Duration T_{14} (hours)	1.42 ± 0.10
Orbital Eccentricity e	0 (fixed)
Planet c	
Orbital Period P_c (days)	$10.778853_{-0.000029}^{+0.000028}$
Mid-Transit Time T_c (BJD)	$2458527.05825_{-0.00052}^{+0.00053}$
Radius Ratio R_p/R_*	$0.0320_{-0.0012}^{+0.0011}$
Impact Parameter b	0.3 ± 0.2
Duration T_{14} (hours)	4.04 ± 0.26
Orbital Eccentricity e	0 (fixed)
Planet d	
Orbital Period P_d^\dagger (days)	$16.37159_{-0.00016}^{+0.00015}$
Mid-Transit Time T_c (BJD)	$2458521.8667_{-0.0012}^{+0.0013}$
Radius Ratio R_p/R_*	$0.0256_{-0.0017}^{+0.0016}$
Impact Parameter b	0.4 ± 0.2
Duration T_{14} (hours)	4.45 ± 0.46
Orbital Eccentricity e	0 (fixed)

[†]Note that an alias of the orbital period of planet d, $P_d = 8.19$ days, is also consistent with the data.

quadratic limb-darkening law as parameterized by [Kipping \(2013\)](#). We allowed the coefficients q_1, q_2 to vary in different photometric bands. We then performed a Monte Carlo Markov Chain analyses with the **Python** package **emcee** (Foreman-Mackey) to sample the posterior distribution of the various transit parameters. The results are summarized in Table 2, and Figure 4 shows the best-fit transit models. We note that the mean stellar density constrained from the transit fit in Table 2 is approximately 1.9σ lower than the mean density listed in Table 1. We attribute this to a possible slight underestimate of the stellar radius (see Section 3.2) or a mild eccentricity that is not included in our transit fit. The difference does not significantly affect our main conclusions since the planet density errors are dominated by uncertainties in the planet masses (see §7).

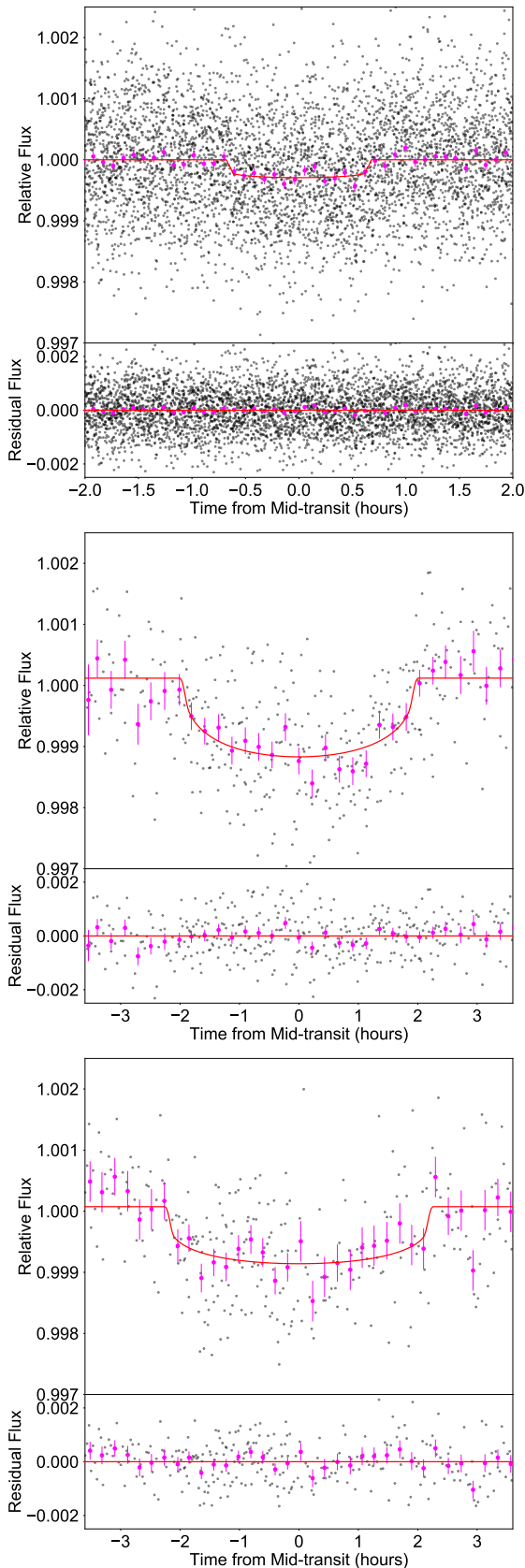


Figure 4. The phase-folded *TESS* transits of TOI-561 planets b (top), c (middle), and d (bottom). The photometry at 2-minute cadence is shown in black, the magenta points show binned fluxes. The red solid line shows the best-fit transit models.

The gap in the *TESS* photometry creates aliasing, allowing the period of the third planet ($P = 16$ days) to instead be half the period, with a missed transit in the gap. The ground-based photometry in which partial transits of planet d were recovered was based on a presumed orbit of $P = 16$ days (since that was the value reported by the SPOC pipeline), and so the current ground-based photometry is not sufficient to resolve the aliasing. Future observations may rule out or validate the $P = 8$ day solution.

We tried models with both $P_d = 16$ and $P_d = 8$ days and ascertained that they performed comparably well. However, the duration of planet d is about 4.6 hours, which, given the host star density (discussed in §3), is more consistent with a circular orbit for $P = 16.4$ days than for $P = 8$ days. We discuss further efforts to disambiguate the orbital period with radial velocities (§6) and stability arguments (§8).

5. HIGH-RESOLUTION IMAGING

As part of our standard process for validating transiting exoplanets to assess the possible contamination of bound or unbound companions on the derived planetary radii (Ciardi et al. 2015) and search for possible sources of astrophysical false positives (e.g., background eclipsing binaries), we obtained high-angular resolution imaging in the near-infrared and optical.

5.1. Gemini-North and Palomar

We utilized both Gemini-North with NIRI (Hodapp et al. 2003) and Palomar Observatory with PHARO (Hayward et al. 2001) to obtain near-infrared adaptive optics imaging of TOI 561, on 24-May-2019 and 08-Jan-2020 respectively. Observations were made in the Br γ filter ($\lambda_o = 2.1686$; $\Delta\lambda = 0.0326\mu\text{m}$). For the Gemini data, 9 dithered images with an exposure time of 2.5s each were obtained; at Palomar, 15 dithered frames with an exposure of 2.8s each were obtained. In both cases, the telescope was dithered by a few arcseconds between each exposure, and the dithered science frames were used to create a sky background. Data were reduced using a custom pipeline: we removed bad pixels, performed a sky background subtraction and a flat correction, aligned the stellar position between images and coadded. The final resolution of the combined dithers was determined from the full-width half-maximum of the point spread function; $0.13''$ and $0.10''$ for the Gemini and Palomar data, respectively.

The sensitivities of the final combined AO images were determined by injecting simulated sources azimuthally around the primary target every 20° at separations of integer multiples of the central source’s FWHM (Furlan

et al. 2017; Lund 2020). The brightness of each injected source was scaled until standard aperture photometry detected it with 5σ significance. The resulting brightness of the injected sources relative to the target set the contrast limits at that injection location. The final 5σ limit at each separation was determined from the average of all of the determined limits at that separation and the uncertainty on the limit was set by the rms dispersion of the azimuthal slices at a given radial distance.

The sensitivity curves are shown in Figure 5 along with an inset image zoomed to the primary target showing no other companion stars. Both the Gemini and Palomar data reach a $\Delta mag \approx 2$ at $0.15''$ with an ultimate sensitivity of 7.7 mag and 8.7 mag for the Gemini and Palomar imaging, respectively. To within the limits and sensitivity of the data, no additional companions were detected.

5.2. SOAR and Gemini-South

We also searched for stellar companions were also searched for with speckle imaging on the 4.1-m Southern Astrophysical Research (SOAR) telescope (Tokovinin et al. 2018) on 18 May 2019 UT. The speckle observations complement the NIR AO as the I-band observations are similar to the TESS bandpass. More details of the observations are available in Ziegler et al. (2020). The observations have a sensitivity of ~ 1 mag at a resolution of $0.06''$ and an ultimate sensitivity of ~ 7 mag at a radius of $3''$. The 5σ detection sensitivity and speckle auto-correlation functions from the observations are shown in Figure 5. As with the NIR AO data, no nearby stars were detected within $3''$ of TOI-561 in the SOAR observations.

High-resolution speckle interferometric images of TOI-561 were obtained on 15 March 2020 UT using the Zorro⁷ instrument mounted on the 8-meter Gemini South telescope located on the summit of Cerro Pachon in Chile. Zorro simultaneously observes in two bands, i.e., 832/40 nm and 562/54 nm, obtaining diffraction limited images with inner working angles $0.''017$ and $0.''026$, respectively. Our data set consisted of 5 minutes of total integration time taken as sets of 1000×0.06 second images. All the images were combined and subjected to Fourier analysis leading to the production of final data products including speckle reconstructed imagery (see Howell et al. 2011). Figure 5 shows the 5σ contrast curves in both filters for the Zorro observation and includes an inset showing the 832 nm reconstructed image. The speckle imaging results reveal TOI-561 to

⁷ <https://www.gemini.edu/sciops/instruments/alopeke-zorro/>

Table 3. Radial Velocities

Time (BJD- T_0)	RV (m s^{-1})	RV unc. (m s^{-1})	S val	Inst
599.74110	4.07	1.32	0.148	HIRES
610.76393	1.39	1.39	0.147	HIRES
617.75783	-1.75	1.41	0.142	HIRES
622.74653	2.27	1.27	0.146	HIRES
623.75467	-2.72	1.41	0.146	HIRES

NOTE—Times are based on $T_0 = 2458000$. The first few lines are shown for form and content. The full machine-readable table is available in the online version.

be a single star to contrast limits of 5 to 8 magnitudes, ruling out main sequence stars brighter than late M as possible companions to TOI-561 within the spatial limits of ~ 2 to 103 au (at $d = 86$ pc).

6. RADIAL VELOCITIES

We obtained 59 high-resolution spectra with the W. M. Keck Observatory HIRES instrument on Maunakea, Hawaii between May 2019 and July 2020, at a cadence of one to two RVs per night. We followed the standard observing and data reduction procedures of the California Planet Search (CPS, Howard et al. 2010). We obtained spectra with the C2 decker, which has dimensions of $14'' \times 0.''86$ and spectral resolution $R \approx 60,000$ at 500 nm. We only observed when the target was at least 25° from the moon. At $V = 10.2$, the star was always at least 8 magnitudes brighter than the moon-illuminated background sky.

We placed a warm cell of molecular iodine gas in the light path as a simultaneous wavelength calibration source for all RV spectra (Marcy & Butler 1992). We obtained a template spectrum by observing the star without the iodine cell. We observed rapidly-rotating B stars, with the iodine cell in the light path, immediately before and after the template to model the PSF of the HIRES spectrograph. Each RV spectrum was forward modeled as a combination of the deconvolved template spectrum and a laboratory iodine atlas spectrum convolved with the HIRES PSF of the observation (which we empirically determined). The RVs are listed in Table 3 and displayed in Figure 6. Before fitting for any planets, the RVs had an RMS of 5.0 m s^{-1} , and the median individual RV error (before applying jitter) was 1.4 m s^{-1} .

When fitting RVs, the mass and density determinations of small planets can sensitively depend on the

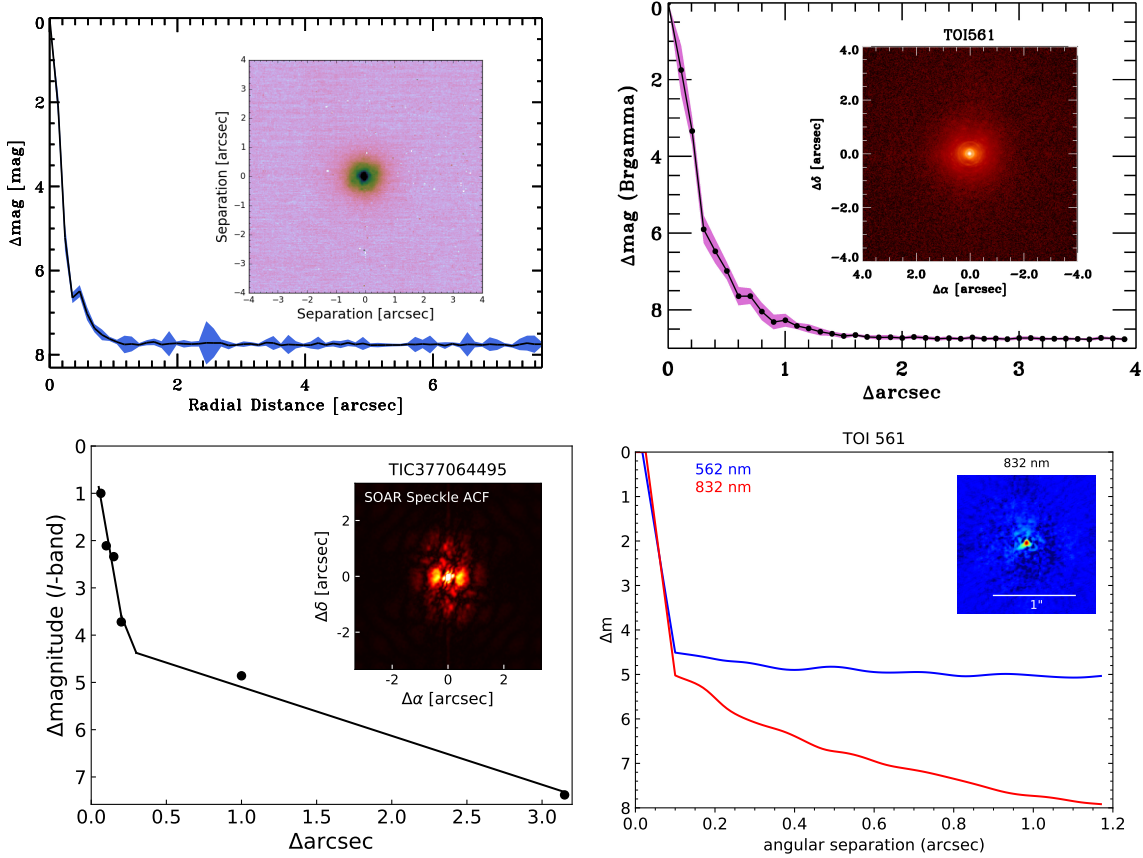


Figure 5. No nearby stars were detected in 4 independent imaging campaigns. Top left: Sensitivity to background stars of our Gemini-N/NIRI images in the Br γ filter. The images were taken in good seeing conditions, and we reach a contrast of 7.5 magnitudes fainter than the host star within 0.''5. *Inset:* Image of the central portion of the data, centered on the star. Top right: Same as top left, but with Palomar. Bottom left: sensitivity to background stars from SOAR speckle imaging observations (5- σ upper limits), with an example image inset. Bottom right: Same as bottom left, but with Gemini-S/Zorro in two passbands.

choice of model, particularly the number of planets included and their orbital periods and the use or non-use of correlated noise models. For example, in the Kepler-10 system, the measured mass of Kepler-10 c ranged from 7 to 17 M_{\oplus} , based on the choice of model (Dumusque et al. 2014; Weiss et al. 2016; Rajpaul et al. 2017). To test the robustness of our mass and density determinations, we applied several different models to the RVs of TOI-561.

6.1. Three-Planet Keplerian Models

We modeled the RVs with the publicly available python package `radvel` (Fulton et al. 2018). We modeled each planet with a five-parameter Keplerian orbit, in which the RV component of each planet is described by its orbital period (P), time of conjunction (T_c), eccentricity (e), argument of periastron passage (ω), and RV semi-amplitude (K). Because the orbital ephemerides from *TESS* are more precise than what we can constrain with 59 RVs, we fixed P and T_c for each transiting planet

at the best-fit values from *TESS* photometry plus additional ground-based photometry from the *TESS* Science Group 1.⁸

The eccentricities of all three planets are expected to be small for dynamical reasons. At $P < 1$ day, the USP is almost certainly tidally circularized. The other planets have compact orbits ($P_d/P_c \approx 1.5$), such that large eccentricities would result in orbit crossings, and even modest eccentricities would likely result in Lagrange instability (Deck et al. 2013). Furthermore, the majority of small exoplanets in compact configurations have low eccentricities (Van Eylen et al. 2019; Mills et al. 2019). For these reasons, and also because modeling eccentricities introduces two free parameters per planet, we only explored circular fits for all three transiting planets.

⁸ We also tried allowing the periods and transit ephemerides to vary but with priors from the best-fit ephemeris, without substantial difference to the results.

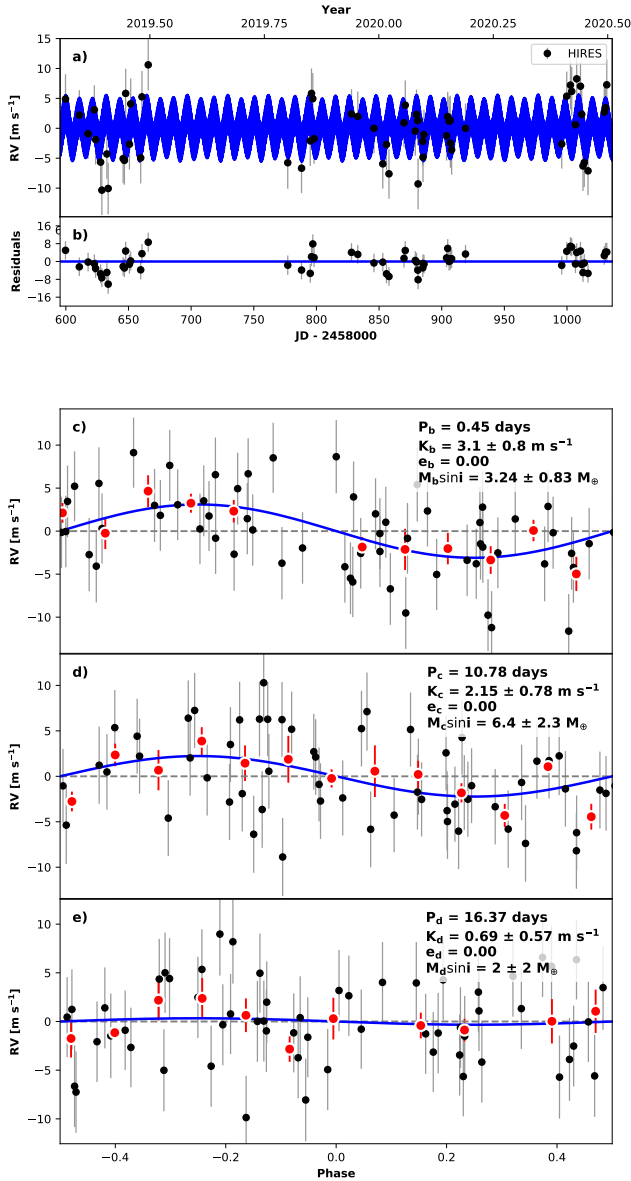


Figure 6. Radial velocities of TOI-561, based on observations from Keck-HIRES (black points). Error bars are 1σ confidence intervals, and the blue line is the best-fit model. The top panel is the full RV time series and residuals. Subsequent panels are the RVs components of planets b, c, and d, phase-folded to the orbital period of each planet (the model RV components from the other planets are subtracted from each panel). The red points are RVs binned in phases of 0.1.

Thus, of the five Keplerian parameters that describe each transiting planet, only the semi-amplitude (K) was allowed to vary, along two global terms: an RV zeropoint offset (γ) and an RV jitter (σ_j), which is added to the individually determined RV errors in quadrature to ac-

count for non-Gaussian, correlated noise in the RVs from stellar processes and instrumental systematics. Our full likelihood model was:

$$-2\ln\mathcal{L} = \sum_i \frac{(x_{\text{meas},i} - x_{\text{mod},i})^2}{\sigma_i'^2} + \sum_i \ln(2\pi\sigma_i'^2) \quad (2)$$

where

$$\sigma_i'^2 = \sigma_i^2 + \sigma_j^2 \quad (3)$$

is the quadrature sum of the internal RV error and the jitter.

We optimized the likelihood function with the Powell method and used a Markov-Chain Monte Carlo (MCMC) analysis⁹ to determine parameter uncertainties. We explored the optimization of several models. In Model A, we did not enforce any priors on planet semi-amplitudes (thus allowing values of K , and hence planet mass, to be negative). Although negative planet masses are unphysical, their consideration offsets the bias toward high planet masses that occurs when planet masses are forced to be positive (Weiss & Marcy 2014). The best-fit values with Model A were $K_b = 3.1 \pm 0.8 \text{ m s}^{-1}$, $K_c = 2.2 \pm 0.8 \text{ m s}^{-1}$, and $K_d = 0.3 \pm 0.8 \text{ m s}^{-1}$. The RMS of the RV residuals was 4.2 m s^{-1} .

In Model B, we restricted $K > 0$. The advantages of restricting planet masses to be larger than zero are (1) the planet masses are physically motivated, and (2) the residuals are more likely to be useful in searching for additional planets. Model B yielded $K_b = 3.1 \pm 0.8 \text{ m s}^{-1}$, $K_c = 2.1 \pm 0.8 \text{ m s}^{-1}$, and $K_d = 0.7^{+0.7}_{-0.5} \text{ m s}^{-1}$. The RMS of the RV residuals was 4.2 m s^{-1} .

Model C was the same as Model B, except we allowed a linear trend in the RVs, $\dot{\gamma}$, which could be caused by acceleration from a long-period companion. However, the RVs do not strongly favor a trend: $\dot{\gamma} = 0.009 \pm 0.004 \text{ m s}^{-1} \text{ ms}^{-1} \text{ day}^{-1}$, and the best-fit K values changed by less than 1σ with the inclusion of a trend: $K_b = 3.2 \pm 0.8 \text{ m s}^{-1}$, $K_c = 2.1 \pm 0.8 \text{ m s}^{-1}$, and $K_d = 1.0^{+0.7}_{-0.6} \text{ m s}^{-1}$. The RMS of the RV residuals was 4.0 m s^{-1} .

In Model D, we considered the hypothesis that planet d has half of the presumed orbital period, which was possible given the gap in the photometry. This model is the same as Model B, except $P_d = 8.2$ days. This model did not affect the amplitudes of planets b or c, but resulted in $K_d < 2.04 \text{ m s}^{-1}$ (2σ confidence). The RMS of the RV residuals was 4.1 m s^{-1} .

In Models A-C, the choice of model makes very little impact on the best-fitting RV semi-amplitudes for each planet, and hence our planet mass determinations are

⁹ based on `emcee`, Foreman-Mackey et al. (2013)

Table 4. 3-Planet Keplerian MCMC Posteriors (Model B)

Parameter	68% C.I.	Max. Likelihood	Units
P_b	$\equiv 0.4466$	$\equiv 0.4466$	days
T_{conj_b}	$\equiv 517.4989$	$\equiv 517.4989$	TKJD
e_b	$\equiv 0.0$	$\equiv 0.0$	
ω_b	$\equiv 0.0$	$\equiv 0.0$	radians
K_b	$3.13^{+0.79}_{-0.78}$	3.1	m s^{-1}
P_c	$\equiv 10.7783$	$\equiv 10.7783$	days
T_{conj_c}	$\equiv 527.0553$	$\equiv 527.0553$	TKJD
e_c	$\equiv 0.0$	$\equiv 0.0$	
ω_c	$\equiv 0.0$	$\equiv 0.0$	radians
K_c	$2.13^{+0.78}_{-0.77}$	2.23	m s^{-1}
P_d^\dagger	$\equiv 16.3713$	$\equiv 16.3713$	days
T_{conj_d}	$\equiv 521.8648$	$\equiv 521.8648$	TKJD
e_d	$\equiv 0.0$	$\equiv 0.0$	
ω_d	$\equiv 0.0$	$\equiv 0.0$	radians
K_d	$0.69^{+0.69}_{-0.47}$	0.33	m s^{-1}
γ	$\equiv -0.8291$	$\equiv -0.8291$	m s^{-1}
$\dot{\gamma}$	$\equiv 0.0$	$\equiv 0.0$	$\text{m s}^{-1} \text{d}^{-1}$
$\ddot{\gamma}$	$\equiv 0.0$	$\equiv 0.0$	$\text{m s}^{-1} \text{d}^{-2}$
σ_j	$4.09^{+0.49}_{-0.42}$	3.91	m s^{-1}

TKJD = BJD - 2458000.0

[†]Note that an alias of the orbital period of planet d, $P_d = 8.19$ days, is also consistent with the data.

robust with respect to our choice of model. For the rest of this paper, we consider Model B as our default model unless stated otherwise. The fitted and fixed parameters of Model B are provided in Table 4.

6.2. Correlated Noise Analysis

The simple Keplerian model fit to observed RVs of TOI-561 displayed a substantial red noise component, with the RV residuals having an RMS of 4.2 m s^{-1} (Figure 6). We considered several correlated-noise models in an attempt to model and remove the red noise component. In Model E, we employed Gaussian process regression (GP), which has been previously applied in analysing RVs of many exoplanets (e.g. Haywood et al. 2014; Grunblatt et al. 2015). For details of the GP model, see Dai et al. (2017). In principle, the light curve and RVs are both affected by stellar activity rotating in and out of view of the observer (e.g., Aigrain et al. 2012). In an attempt to model the correlated noise in the RVs, we trained the various “hyperparameters” of our GP quasi-periodic kernel using the out-of-transit *TESS* PDCSAP light curve. We note that the stellar rotation period was not detected in the *TESS* PDCSAP light

curve, possibly because the pre-data conditioning algorithm can unintentionally remove stellar variability on timescales longer than 10 days, the star is very inactive ($\log R'_{\text{HK}} = -5.1$), or the expected rotation period of the star is longer than the photometric baseline. We visually inspected the SAP flux for comparison, but it had a large systematic from a data downlink and no clear rotation period. Our MCMC fit to the lightcurve produced broad posteriors on the rotation period and the other hyperparameters. We used EMCEE to constrain the posterior distribution of the GP hyperparameters simultaneously with the orbital parameters of the three planets. We detect the RV signal of planet b: $K_b = 2.9 \pm 0.7 \text{ m s}^{-1}$ and planet c: $K_b = 1.7 \pm 1.0$ and an upper limit for planet d: $K_d < 1.6 \text{ m s}^{-1}$ (95% confidence), all of which are within 1σ of the planet semi-amplitudes we determined without the correlated noise component of the model.

We also attempted to train a correlated noise model on our spectroscopically determined Mt. Wilson S-values. The S-values are not sampled as frequently as the lightcurve, but they are sampled simultaneously with the RVs, and they are a direct indicator of the chromospheric magnetic activity during the observations. Our Lomb-Scargle periodogram of the S-values produces peaks at 230 and 100 days, either of which might be the rotation period of the old, K dwarf star. We tried a GP with a quasi-periodic kernel trained on the S-values (Model F), but this did not produce significant changes in the semi-amplitudes of the planets or the RMS of the RV residuals, possibly because the S-values had small variability or were sparsely sampled. We also tried a model in which we decorrelated the RVs with respect to the S-values (Model G), which did not reduce the RMS (and thus did not remove the correlated noise).

None of our attempts to model correlated noise in the RVs changed the amplitudes of the planets or reduced the RMS of the RV residuals, and so we prefer the simpler Keplerian models (without correlated noise) described above. Perhaps TOI-561 is too inactive for models trained on stellar activity to be effective, given the current quality of the data. For comparison, Kepler-10, another system with time-correlated RV residuals, has $\log(R'_{\text{HK}} = -4.89)$, which is more active than TOI-561 ($\log(R'_{\text{HK}} = -5.1)$). The use of Gaussian processes affected the mass determination of Kepler-10 c, lowering it from $14 M_{\oplus}$ (no GP) to $7 M_{\oplus}$ (with GP). Perhaps there is a minimum stellar activity for which attempts to decorrelate the stellar activity signal can be successful, given RVs with precision of 2 m s^{-1} .

Nonetheless, there are substantial correlated residuals in the RVs of TOI-561 which are uncharacteristic of the HIRES instrument performance (typically 2 m s^{-1}

Table 5. Derived Planetary Parameters

Parameter	68% C.I.	Max. Likelihood	Units
Planet b			
a_b	0.01064 ± 0.00013	0.01071	AU
R_b	1.45 ± 0.11	1.45	R_\oplus
M_b	$3.24^{+0.83}_{-0.82}$	3.25	M_\oplus
ρ_b	$5.7^{+2.2}_{-1.7}$	6.0	g cm^{-3}
Planet c			
a_c	0.0888 ± 0.0011	0.0894	AU
R_c	2.90 ± 0.13	2.90	R_\oplus
M_c	$6.4^{+2.3}_{-2.4}$	7.0	M_\oplus
ρ_c	$1.44^{+0.58}_{-0.53}$	1.53	g cm^{-3}
Planet d			
a_d	0.1174 ± 0.0015	0.1148	AU
R_d	2.32 ± 0.16	2.32	R_\oplus
M_d	$2.4^{+2.3}_{-1.6}$	1.2	M_\oplus
ρ_d	$1.0^{+1.1}_{-0.7}$	0.5	g cm^{-3}

for $V < 11$, Howard & Fulton 2016). The residual RVs of TOI-561 are not well-explained by any of our models of stellar activity, and so perhaps additional planets contribute to the RV residuals. More RVs are needed to identify the orbital periods of any such planets and model their Keplerian signals.

7. PLANET MASSES & DENSITIES

Each K value can be converted to the planet’s minimum mass, $M_p \sin i$, but because all three planets transit, actual masses (rather than minimum masses) can be calculated. Assuming Model B, we find $M_b = 3.2 \pm 0.8 M_\oplus$, $M_c = 6.5 \pm 2.4 M_\oplus$, and $M_d = 2.4^{+2.3}_{-1.7} M_\oplus$. Furthermore, since the planets transit, their radii are calculated from the planet-to-star radius ratios and known stellar radius: $R_b = 1.45 \pm 0.11 R_\oplus$, $R_c = 2.90 \pm 0.13 R_\oplus$, and $R_d = 2.32 \pm 0.16 R_\oplus$. The bulk densities of the planets are $\rho_b = 5.6^{+2.2}_{-1.7} \text{g cm}^{-3}$, $\rho_c = 1.45 \pm 0.55 \text{g cm}^{-3}$, and $\rho_d = 1.1^{+1.1}_{-0.7} \text{g cm}^{-3}$. The derived physical and orbital properties of the planets are summarized in Table 5.

The masses and densities of the TOI-561 planets are shown in comparison to the masses and densities of other sub-Neptune sized planets in Figure 7. The other planet masses and densities come from the NASA Exoplanet Archive, from which we included only those with $\sigma(M_p) < 2 M_\oplus$.

7.1. TOI-561 b

The USP TOI-561 b has a typical mass and density for its size. At $1.5 R_\oplus$ and $5.6^{+2.2}_{-1.7} \text{g cm}^{-3}$, it is 1σ below the peak of the density-radius diagram identified in Weiss & Marcy (2014), consistent with a rocky composition that is either Earth-like or iron-poor. Nearly all USPs are smaller than $2 R_\oplus$ and are expected to have rocky compositions, given their small sizes and extreme stellar irradiation (Sanchis-Ojeda et al. 2015), and TOI-561 b is consistent with this expectation. In a homogeneous analysis of USPs with masses determined from RVs, Dai et al. (2019) found that most USPs with $< 10 M_\oplus$ are consistent with having Earth-like compositions, whereas the few USPs with $> 10 M_\oplus$ likely have H/He envelopes. TOI-561 b ($3.2 \pm 0.8 M_\oplus$) is consistent with the rocky group of that study.

The minimum density of a USP can be determined from its orbital period and the requirement that it orbits outside the Roche limiting distance (Rappaport et al. 2013). We investigated the minimum density of TOI-561 b, with the hope that it would provide additional constraints on the mass of the planet. Using the approximation from Sanchis-Ojeda et al. (2014), we find that the minimum density of the USP is

$$\rho_p [\text{g cm}^{-3}] \geq (11.3 \text{hr}/P_{\text{orb}})^2 = 1.15 \text{g cm}^{-3} \quad (4)$$

for TOI-561 b, which is below our measured density and corresponds to a minimum mass of $0.64 M_\oplus$. Such a low mass is ruled out by the data at nearly 3σ confidence. Thus, TOI-561 b is not close enough to its star for the Roche stability criterion to provide additional information about the density.

7.2. TOI-561 c & d

At $R_p > 1.5 R_\oplus$ and with low densities, TOI-561 c and d have substantial gaseous envelopes by volume, although the gas envelopes likely only constitute $\sim 1\%$ of the planet masses (Lopez & Fortney 2014). TOI-561 c has a radius and mass consistent with the Weiss & Marcy (2014) empirical mass-radius relationship.

The ambiguity of the orbital period for planet d poses a challenge to accurate mass determination. Our RVs are consistent with a non-detection of planet d at both the $P_d = 16$ and $P_d = 8$ day orbits. Assuming $P_d = 16$ days, the RVs provide an upper limit of $K_d < 2.1 \text{m s}^{-1}$, which corresponds to $M_p < 7.0 M_\oplus$ (2σ confidence, see §6). Assuming $P_d = 8$ days, the RVs provide an upper limit of $K < 2.0 \text{m s}^{-1}$, which corresponds to $M_p < 5.6 M_\oplus$ (2σ confidence). In either scenario, the mass of TOI-561 d is approximately 2σ below the Weiss & Marcy (2014) mass-radius relationship and is too low to be consistent with a rocky composition, given the planet’s radius.

As an ensemble, planets b, c, and d have lower masses (and densities) than expected from the [Weiss & Marcy \(2014\)](#) relationship. Planet b is 1σ below the relation, planet c is on the relation, and planet d is 2σ below the relation, and so as an ensemble they are $\approx \sqrt{1^2 + 0^2 + 2^2} = 2.2\sigma$ below the expected densities for planets of their sizes. The below-average densities of these planets suggests that their rocky cores are iron-poor, correlating with the host star’s below-average iron content.

7.3. Non-Detection of Outer Giant Planets

With our year-long baseline of RVs, we were able to place constraints on possible long-period giant planets. In Model C, we found a 3σ upper limit to an RV trend of $\dot{\gamma} < 0.02 \text{ m s}^{-1} \text{ day}^{-1}$. This observational limit on the acceleration of the star can be converted to a limit on the mass and orbital distance of a possible perturber by setting it equal to the gravitational acceleration from a planet at distance r : $GM_{\star}M_{\text{p}}r^{-2} = M_{\star}\dot{\gamma}$, where G is the gravitational constant and r is the distance between the perturber and the star at the time the RVs were measured. Assuming a circular orbit for the putative giant planet ($r = a$), we find

$$\frac{M_{\text{p}} \sin i}{M_{\text{J}}} \left(\frac{a}{5\text{AU}}\right)^{-2} < 1.1 \quad (5)$$

(3σ confidence). Thus, our non-detection of an RV acceleration rules out a $1.1 M_{\text{J}}$ planet at 5 AU with 3σ confidence (assuming $\sin i \approx 1$, $e = 0$, and that we did not primarily sample the orbit while the planet was moving parallel to the sky plane). In systems with compact configurations of transiting planets, giant planets often need to be approximately coplanar with the transiting planets in order for the inner planets to remain mutually continuously transiting ([Becker & Adams 2017](#)), and so we do not expect non-transiting companions to have face-on orbits. Thus, the non-detection of an RV trend rules out a variety of scenarios of a coplanar giant planet near the snow-line.

8. DISCUSSION

8.1. Stability

We investigated whether we could constrain the architecture of the TOI-561 system, and in particular the orbital period of planet d, with stability arguments. To assess stability, we used *Spock*, a machine-learning based approach to inferring orbital stability ([Tamayo et al. 2020](#)). *Spock* incorporates several analytic indicators (including MEGNO, AMD, and Mutual Hill radius) with an N-body integration of 10^4 orbits to compute a probabilistic assessment of the system stability.

We tested the architectures of TOI-561 with planet d at $P_d = 16.4$ days (Model B) and at $P_d = 8.2$ days (Model D). We assumed all three transiting planets were coplanar and initialized the planets with zero eccentricity. For both Model B and Model D, the probability that the configuration is stable is $> 95\%$. Thus, we cannot rule out Model D based on a stability argument.

8.2. Formation and Evolution

TOI-561 is the second transiting multiplanet system discovered around a galactic thick-disk star ([Kepler-444](#), [Campante et al. 2015](#), is the first), and is the first galactic thick disk star with a USP. The iron-poor, alpha-enhanced stellar abundances observed today are likely representative of the nebular environment in which the planets formed. Thus, TOI-561 provides an opportunity to study the outcome of planet formation in an environment that is chemically distinct from most of the planetary systems known to date. Furthermore, its membership in the galactic thick disk indicates old age, making the rocky planet TOI-561 b one of the oldest rocky planets known.

The confirmed old age of the system is relevant for dynamical studies of the planets. For instance, the formation of USPs is still poorly understood. The majority of USPs are the only detected transiting planet in their systems ([Sanchis-Ojeda et al. 2014](#)). This is partially due to a bias of geometry (as planet detection probability scales with R_{\star}/a). However, [Dai et al. \(2018\)](#) found that the mutual inclinations in multiplanet systems with USPs are significantly larger than in the multiplanet systems without USPs, suggesting that systems with USPs have had more dynamically “hot” histories. One mechanism for generating large mutual inclinations in systems with USPs is if the host star is oblate and misaligned with respect to the planets ([Li et al. 2020](#)).

Furthermore, dynamical interactions in a multiplanet system can move short-period planets to ultra-short periods in a manner that may excite large eccentricities. [Petrovich et al. \(2019\)](#) proposed a mechanism of secular chaos in which the innermost planet is kicked to a high-eccentricity orbit, which is then circularized. In contrast, [Pu & Lai \(2019\)](#) proposed a scheme in which the innermost planet’s neighbors consistently force it to a low-eccentricity orbit, which results in inward migration and eventual circularization.

In a study of the Gaia-DR2 kinematics of USP host stars in the *Kepler* field, [Hamer & Schlaufman \(2020\)](#) found that their motions are similar to those of matched field stars (rather than young stars). The broad range of ages of USPs suggests that USPs do not undergo rapid tidal inspiral during the host star’s main sequence life-

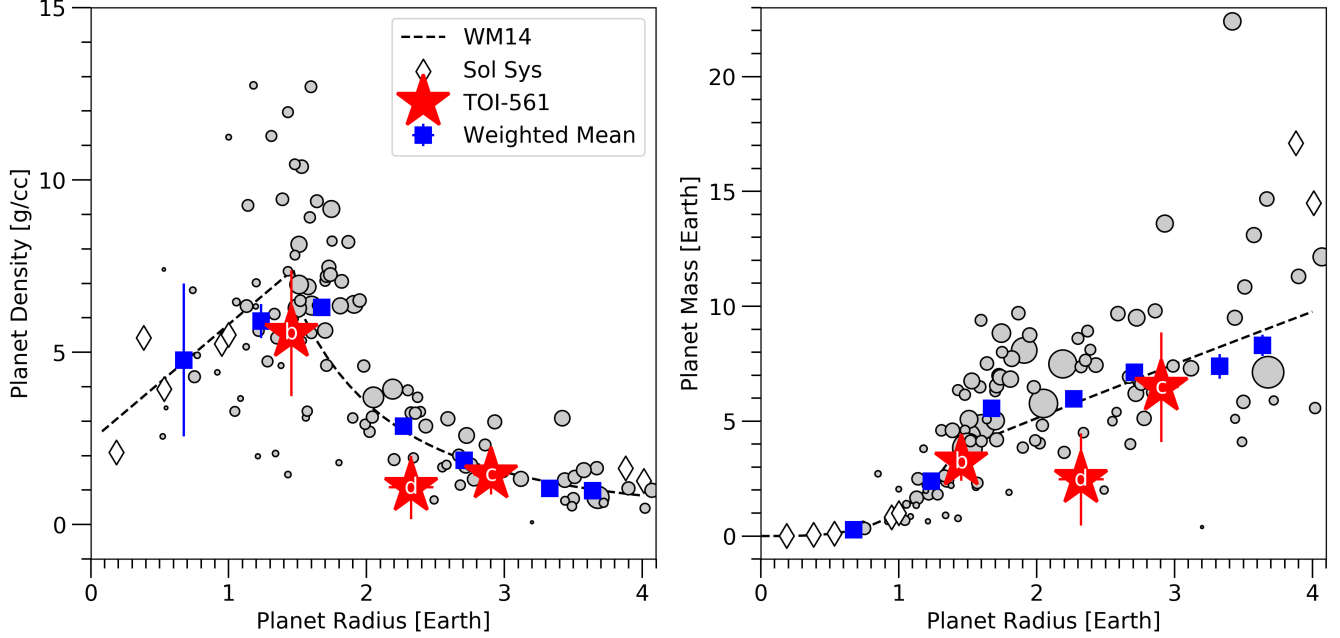


Figure 7. Left: Planet bulk density vs. planet radius for small planets with measured radii ($R_p < 4 R_\oplus$, $\sigma(R_p)/R_p < 0.2$) and masses ($\sigma(M_p) < 2 M_\oplus$), based on results from the NASA Exoplanet Archive (queried 2020 June 24 [Akeson et al. 2013](#), gray points). The point size is scaled to $\rho_p/\sigma(\rho_p)$. Weighted mean densities in bins of $0.5 R_\oplus$ (blue squares) and the [Weiss & Marcy \(2014\)](#) mass-radius relationship (black dashed line), and solar system planets and Earth’s moon (white diamonds) are provided for context of the TOI-561 planets (labeled red stars). The planets are consistent with or slightly less dense than typical planets of their sizes.

time. The existence of USP around an 10 Gyr old star is consistent with this finding.

8.3. Predicted Transit Timing Variations

Because planets c and d have an orbital period ratio of ~ 1.5 or less, the planets likely perturb each other’s orbits, producing transit timing variations (TTVs). The *TESS* sector 8 baseline was too short to detect TTVs (only two transits of each planet were detected). The approximate amplitude of the TTV signal can be computed analytically using the expressions from [Lithwick et al. \(2012\)](#):

$$|V| \approx P\mu'/\Delta + \mathcal{O}(e)/\Delta \quad (6)$$

where P is the orbital period of the inner planet, μ' is the mass of the perturbing, outer planet (in units of stellar mass), $\mathcal{O}(e)$ is a first-order dependency on the free eccentricities of the planets, and Δ is the non-dimensional distance from mean motion resonance:

$$\Delta = \frac{P'}{P} \frac{j-1}{j} - 1 \quad (7)$$

where P and P' are the inner and outer orbital periods and j is an integer. Equation 6 can be used to approximate the TTV amplitude of the outer planet by setting

$P \rightarrow P'$ and $\mu' \rightarrow \mu$ (for a thorough derivation and caveats, see [Lithwick et al. 2012](#)).

Using the values for the planet masses determined in §7 and assuming circular orbits, we find that the TTV amplitude of planet c ($P = 10.78$ days) is about 6 minutes, whereas the TTV amplitude of planet d is either 30 minutes (if $P_d = 16.4$ days; $j = 3$) or 15 minutes (if $P_d = 8.2$ days, $j = 4$).

8.4. Remote Sensing Possibilities

Using the system parameters tabulated in this paper, we calculated the Transmission and Emission Spectroscopy Metrics (TSM and ESM, respectively) of [Kempton et al. \(2018\)](#) to determine whether these newly-characterized planets are compelling targets for future atmospheric or surface characterization via transit or eclipse spectroscopy. Because of the relatively shallow transit depths ($\lesssim 1000$ ppm for all three planets), space-based spectroscopy is likely to be the only feasible avenue for such studies. In contrast to some recent reports of these quantities for other newly-discovered *TESS* planets, here we propagate all parameter uncertainties in order to report how well the TSM and ESM are constrained, as well as how promising the median values are; this is especially essential when planetary properties are not yet measured to high precision.

We report the transmission and emission metrics and their uncertainties in Table 6.

Our analysis shows that TOI-561 b is among the best *TESS* targets discovered to date for thermal emission measurements (cf. Table 3 of [Astudillo-Defru et al. 2020](#)). With $\text{ESM} = 7.1 \pm 1.1$, planet b is clearly a promising target for observations of its secondary eclipse and/or its full-orbit phase curves, as has previously been done for other irradiated terrestrial planets such as 55 Cnc e ([Demory et al. 2012, 2016](#)) and LHS 3844b ([Kreidberg et al. 2019](#)). The uncertainty on planet b’s ESM is dominated by the uncertainty on its transit depth, but regardless the planet has a reliably high metric in this category. Because of their cooler temperatures, the lower ESM values for planets b and c mark them as less attractive targets for secondary eclipse studies.

As for transit spectroscopy, the TSM values for the sub-Neptunes TOI-561c and d listed in Table 6 (97 ± 42 and 71 ± 50 , respectively) indicate that they *may* be particularly amenable to transmission studies. However, because the TSM scales inversely with planetary surface gravity this result depends on determining more precise values of these planets’ masses. These planets clearly warrant additional precise RV followup: if the expectation values of their TSMs do not change as the uncertainties shrink, these two planets would be among the top 20 confirmed warm Neptunes for transmission spectroscopy (cf. Table 11 of [Guo et al. 2020](#)). Due to the small size of the highly irradiated planet b, and because it is unlikely to have retained much of an atmosphere, it is not an appealing target for transmission measurements.

Better ephemerides for planets c and d are necessary in preparation for atmospheric studies. The alias of the orbit of planet d should be resolved prior to interpretation of the planetary atmospheres, since the factor of two change in orbital period produces a factor of ~ 1.3 change in the equilibrium temperature. Also, planet d may have significant TTVs with amplitudes of ~ 30 minutes (assuming the orbital period is 16.4 days).

9. CONCLUSION

TOI-561 is system with three transiting planets identified by the NASA *TESS* spacecraft and confirmed with ground-based follow-up. In particular:

1. TOI-561 is a metal-poor, alpha-enhanced member of the galactic thick disk ($[\text{Fe}/\text{H}] = -0.4$, $\alpha = 0.2$). It is one of the oldest planetary systems yet identified and one of the most metal-poor. In both of these aspects it is an important benchmark in our understanding of planet formation and evolution.

Table 6. Atmospheric Prospects

Planet	TSM	ESM	Notes
b	7.3 ± 2.5	7.1 ± 1.1	Good eclipse target
c	97 ± 42	3.9 ± 0.3	Promising transmission target
d [†]	71 ± 50	1.6 ± 0.2	Promising transmission target

[†] Assuming $P_d = 16$ days. If $P_d = 8$ days then $\text{TSM}_d = 100^{+320}_{-10}$ (68% confidence interval).

2. With ground-based transit photometry, we determined that other stars within $2.5'$ of TOI-561 are not the source of the transit signals. With high-resolution imaging, we ruled out the presence of stars with $\Delta\text{mag} < 2$ at a separation of $0.''15$ from TOI-561. Our speckle imaging ruled out main sequence stellar companions brighter than late M between 2 and 130 au. These non-detections rule out astrophysical false positive scenarios and validate the TOI-561 planets as bona-fide.
3. With 59 RVs from Keck-HIRES, we determined the mass and density of the ultra-short period rocky planet TOI-561 b: $M_b = 3.2 \pm 0.8 M_{\oplus}$, $\rho_b = 5.6^{+2.2}_{-1.7} \text{ g cm}^{-3}$. We also determined mass upper limits for transiting sub-Neptune sized planets c and d, with best-fit masses of $M_c = 6.5 \pm 2.4 M_{\oplus}$ and $M_d = 2.4^{+2.3}_{-1.7} M_{\oplus}$. As an ensemble, the planets have lower-than-average masses for their sizes (2.2σ confidence), suggesting their rocky cores may be iron-poor.
4. The RVs from Keck-HIRES span a full year and do not have a significant trend. The non-detection of a trend rules out various scenarios of a giant planet near the ice line. For instance, a planet of $M_p \sin i = 1.1 M_J$ at 5 AU is ruled out with 3σ confidence.
5. Thanks to the bright host star, this multi-planet system is amenable to atmospheric follow-up with space-based telescopes. Planet b is expected to be a good eclipse target, while planets c and d are promising targets for transmission spectroscopy. Comparative atmospheric properties for the planets in this very metal-poor system would provide a unique test for planet formation scenarios.

We thank the time assignment committees of the University of California, the California Institute of Technology, NASA, and the University of Hawaii for supporting

the TESS-Keck Survey with observing time at Keck Observatory and on the Automated Planet Finder.

We thank NASA for funding associated with our Key Strategic Mission Support project. We gratefully acknowledge the efforts and dedication of the Keck Observatory staff for support of HIRES and remote observing. We recognize and acknowledge the cultural role and reverence that the summit of Maunakea has within the indigenous Hawaiian community. We are deeply grateful to have the opportunity to conduct observations from this mountain.

We thank Ken and Gloria Levy, who supported the construction of the Levy Spectrometer on the Automated Planet Finder. We thank the University of California and Google for supporting Lick Observatory and the UCO staff for their dedicated work scheduling and operating the telescopes of Lick Observatory. This paper is based on data collected by the TESS mission. Funding for the TESS mission is provided by the NASA Explorer Program. We acknowledge the use of public *TESS* Alert data from pipelines at the *TESS* Science Office and at the *TESS* Science Processing Operations Center. We thank David Latham for organizing the TESS community follow-up program, which brought together the widespread authorship and diversity of resources presented in this manuscript.

Observations in the paper made use of the High-Resolution Imaging instrument ‘Alopeke. ‘Alopeke was funded by the NASA Exoplanet Exploration Program and built at the NASA Ames Research Center by Steve B. Howell, Nic Scott, Elliott P. Horch, and Emmett Quigley. ‘Alopeke was mounted on the Gemini North telescope of the international Gemini Observatory, a program of NSF’s OIR Lab, which is managed by the Association of Universities for Research in Astronomy (AURA) under a cooperative agreement with the National Science Foundation on behalf of the Gemini partnership: the National Science Foundation (United States), National Research Council (Canada), Agencia Nacional de Investigación y Desarrollo (Chile), Ministerio de Ciencia, Tecnología e Innovación (Argentina), Ministério da Ciência, Tecnologia, Inovações e Comunicações (Brazil), and Korea Astronomy and Space Science Institute (Republic of Korea).

This work makes use of observations from the LCOGT network. This article is based on observations made with the MuSCAT2 instrument, developed by ABC, at Telescopio Carlos Sánchez operated on the island of Tenerife by the IAC in the Spanish Observatorio del Teide. This work is partly supported by JSPS KAKENHI Grant Numbers JP17H04574, JP18H01265 and JP18H05439, and JST PRESTO Grant Number JPMJPR1775.

This research has made use of the Exoplanet Follow-up Observing Program (ExoFOP), which is operated by the California Institute of Technology, under contract with the National Aeronautics and Space Administration. Resources supporting this work were provided by the NASA High-End Computing (HEC) Program through the NASA Advanced Supercomputing (NAS) Division at Ames Research Center for the production of the SPOC data products.

L.M.W. is supported by the Beatrice Watson Parrent Fellowship and NASA ADAP Grant 80NSSC19K0597. D.H. acknowledges support from the Alfred P. Sloan Foundation, the National Aeronautics and Space Administration (80NSSC18K1585, 80NSSC19K0379), and the National Science Foundation (AST-1717000). E.A.P. acknowledges the support of the Alfred P. Sloan Foundation. C.D.D. acknowledges the support of the Hellman Family Faculty Fund, the Alfred P. Sloan Foundation, the David & Lucile Packard Foundation, and the National Aeronautics and Space Administration via the *TESS* Guest Investigator Program (80NSSC18K1583). I.J.M.C. acknowledges support from the NSF through grant AST-1824644. Z.R.C. acknowledges support from the TESS Guest Investigator Program (80NSSC18K18584). A.C. acknowledges support from the National Science Foundation through the Graduate Research Fellowship Program (DGE 1842402). P.D. acknowledges support from a National Science Foundation Astronomy and Astrophysics Postdoctoral Fellowship under award AST-1903811. A.B. is supported by the NSF Graduate Research Fellowship, grant No. DGE 1745301. R.A.R. is supported by the NSF Graduate Research Fellowship, grant No. DGE 1745301. M.R.K. is supported by the NSF Graduate Research Fellowship, grant No. DGE 1339067. J.N.W. thanks the Heising Simons Foundation for support.

Facilities: TESS, KeckI-HIRES, Gemini-North-NIRI, Gemini-South-Zorro, Palomar, SOAR, LCOGT, El Sauce, PEST, MuSCAT2

Software: Python, Astropy, radvel, emcee, Spectra Made Easy, Specmatch, isoclassify, AstroImageJ, lightkurve, spock, kiaukoku

REFERENCES

- Abadi, M. G., Navarro, J. F., Steinmetz, M., & Eke, V. R. 2003, *ApJ*, 591, 499, doi: [10.1086/375512](https://doi.org/10.1086/375512)
- Adibekyan, V. Z., Sousa, S. G., Santos, N. C., et al. 2012, *A&A*, 545, A32, doi: [10.1051/0004-6361/201219401](https://doi.org/10.1051/0004-6361/201219401)
- Aigrain, S., Pont, F., & Zucker, S. 2012, *MNRAS*, 419, 3147, doi: [10.1111/j.1365-2966.2011.19960.x](https://doi.org/10.1111/j.1365-2966.2011.19960.x)
- Akeson, R. L., Chen, X., Ciardi, D., et al. 2013, *PASP*, 125, 989, doi: [10.1086/672273](https://doi.org/10.1086/672273)
- Astudillo-Defru, N., Cloutier, R., Wang, S. X., et al. 2020, *A&A*, 636, A58, doi: [10.1051/0004-6361/201937179](https://doi.org/10.1051/0004-6361/201937179)
- Becker, J. C., & Adams, F. C. 2017, *MNRAS*, 468, 549, doi: [10.1093/mnras/stx461](https://doi.org/10.1093/mnras/stx461)
- Bensby, T., Feltzing, S., & Lundström, I. 2004, *A&A*, 415, 155, doi: [10.1051/0004-6361:20031655](https://doi.org/10.1051/0004-6361:20031655)
- Bensby, T., Feltzing, S., Lundström, I., & Ilyin, I. 2005, *A&A*, 433, 185, doi: [10.1051/0004-6361:20040332](https://doi.org/10.1051/0004-6361:20040332)
- Bensby, T., Feltzing, S., & Oey, M. S. 2014, *A&A*, 562, A71, doi: [10.1051/0004-6361/201322631](https://doi.org/10.1051/0004-6361/201322631)
- Borucki, W. J., Koch, D., Basri, G., et al. 2010, *Science*, 327, 977, doi: [10.1126/science.1185402](https://doi.org/10.1126/science.1185402)
- Bovy, J., Rix, H.-W., & Hogg, D. W. 2012, *ApJ*, 751, 131, doi: [10.1088/0004-637X/751/2/131](https://doi.org/10.1088/0004-637X/751/2/131)
- Brewer, J. M., Fischer, D. A., Basu, S., Valenti, J. A., & Piskunov, N. 2015, *The Astrophysical Journal*, 805, 126
- Brewer, J. M., Fischer, D. A., Valenti, J. A., & Piskunov, N. 2016, *The Astrophysical Journal Supplement Series*, 225, 32
- Brook, C. B., Kawata, D., Gibson, B. K., & Freeman, K. C. 2004, *ApJ*, 612, 894, doi: [10.1086/422709](https://doi.org/10.1086/422709)
- Brown, T. M., Baliber, N., Bianco, F. B., et al. 2013, *Publications of the Astronomical Society of the Pacific*, 125, 1031, doi: [10.1086/673168](https://doi.org/10.1086/673168)
- Buchhave, L. A., Latham, D. W., Johansen, A., et al. 2012, *Nature*, 486, 375, doi: [10.1038/nature11121](https://doi.org/10.1038/nature11121)
- Campante, T. L., Barclay, T., Swift, J. J., et al. 2015, *ApJ*, 799, 170, doi: [10.1088/0004-637X/799/2/170](https://doi.org/10.1088/0004-637X/799/2/170)
- Carrillo, A., Hawkins, K., Bowler, B. P., Cochran, W., & Vanderburg, A. 2020, *MNRAS*, 491, 4365, doi: [10.1093/mnras/stz3255](https://doi.org/10.1093/mnras/stz3255)
- Casagrande, L., Ramírez, I., Meléndez, J., Bessell, M., & Asplund, M. 2010, *A&A*, 512, A54, doi: [10.1051/0004-6361/200913204](https://doi.org/10.1051/0004-6361/200913204)
- Choi, J., Dotter, A., Conroy, C., et al. 2016, *ApJ*, 823, 102, doi: [10.3847/0004-637X/823/2/102](https://doi.org/10.3847/0004-637X/823/2/102)
- Ciardi, D. R., Beichman, C. A., Horch, E. P., & Howell, S. B. 2015, *ApJ*, 805, 16, doi: [10.1088/0004-637X/805/1/16](https://doi.org/10.1088/0004-637X/805/1/16)
- Clayton, Z. R., van Saders, J. L., Santos, Á. R. G., et al. 2020, *ApJ*, 888, 43, doi: [10.3847/1538-4357/ab5c24](https://doi.org/10.3847/1538-4357/ab5c24)
- Collins, K. A., Kielkopf, J. F., Stassun, K. G., & Hessman, F. V. 2017, *AJ*, 153, 77, doi: [10.3847/1538-3881/153/2/77](https://doi.org/10.3847/1538-3881/153/2/77)
- Dai, F., Masuda, K., & Winn, J. N. 2018, *ApJL*, 864, L38, doi: [10.3847/2041-8213/aadd4f](https://doi.org/10.3847/2041-8213/aadd4f)
- Dai, F., Masuda, K., Winn, J. N., & Zeng, L. 2019, *ApJ*, 883, 79, doi: [10.3847/1538-4357/ab3a3b](https://doi.org/10.3847/1538-4357/ab3a3b)
- Dai, F., Winn, J. N., Gandolfi, D., et al. 2017, *AJ*, 154, 226, doi: [10.3847/1538-3881/aa9065](https://doi.org/10.3847/1538-3881/aa9065)
- Dalba, P. A., Gupta, A. F., Rodriguez, J. E., et al. 2020, *AJ*, 159, 241, doi: [10.3847/1538-3881/ab84e3](https://doi.org/10.3847/1538-3881/ab84e3)
- De Silva, G. M., Freeman, K. C., Bland-Hawthorn, J., et al. 2015, *MNRAS*, 449, 2604, doi: [10.1093/mnras/stv327](https://doi.org/10.1093/mnras/stv327)
- Deck, K. M., Holman, M. J., Agol, E., et al. 2013, *ApJ*, 774, L15, doi: [10.1088/2041-8205/774/1/L15](https://doi.org/10.1088/2041-8205/774/1/L15)
- Demory, B.-O., Gillon, M., Seager, S., et al. 2012, *ApJL*, 751, L28, doi: [10.1088/2041-8205/751/2/L28](https://doi.org/10.1088/2041-8205/751/2/L28)
- Demory, B.-O., Gillon, M., de Wit, J., et al. 2016, *Nature*, 532, 207, doi: [10.1038/nature17169](https://doi.org/10.1038/nature17169)
- Dumusque, X., Bonomo, A. S., Haywood, R. D., et al. 2014, *ApJ*, 789, 154, doi: [10.1088/0004-637X/789/2/154](https://doi.org/10.1088/0004-637X/789/2/154)
- Dupuy, T. J., Kratter, K. M., Kraus, A. L., et al. 2016, *ApJ*, 817, 80, doi: [10.3847/0004-637X/817/1/80](https://doi.org/10.3847/0004-637X/817/1/80)
- Foreman-Mackey, D., Hogg, D. W., Lang, D., & Goodman, J. 2013, *PASP*, 125, 306, doi: [10.1086/670067](https://doi.org/10.1086/670067)
- Fressin, F., Torres, G., Charbonneau, D., et al. 2013, *The Astrophysical Journal*, 766, 81
- Fuhrmann, K. 1998, *A&A*, 338, 161
- Fulton, B. J., Petigura, E. A., Blunt, S., & Sinukoff, E. 2018, *PASP*, 130, 044504, doi: [10.1088/1538-3873/aaaaa8](https://doi.org/10.1088/1538-3873/aaaaa8)
- Furlan, E., Ciardi, D. R., Everett, M. E., et al. 2017, *AJ*, 153, 71, doi: [10.3847/1538-3881/153/2/71](https://doi.org/10.3847/1538-3881/153/2/71)
- Gan, T., Shporer, A., Livingston, J. H., et al. 2020, arXiv e-prints, arXiv:2003.04525. <https://arxiv.org/abs/2003.04525>
- Gilmore, G., & Reid, N. 1983, *MNRAS*, 202, 1025, doi: [10.1093/mnras/202.4.1025](https://doi.org/10.1093/mnras/202.4.1025)
- Grunblatt, S. K., Howard, A. W., & Haywood, R. D. 2015, *ApJ*, 808, 127, doi: [10.1088/0004-637X/808/2/127](https://doi.org/10.1088/0004-637X/808/2/127)
- Guo, X., Crossfield, I. J. M., Dragomir, D., et al. 2020, *AJ*, 159, 239, doi: [10.3847/1538-3881/ab8815](https://doi.org/10.3847/1538-3881/ab8815)
- Hamer, J. H., & Schlaufman, K. C. 2020, arXiv e-prints, arXiv:2007.10944. <https://arxiv.org/abs/2007.10944>
- Hayward, T. L., Brandl, B., Pirger, B., et al. 2001, *PASP*, 113, 105, doi: [10.1086/317969](https://doi.org/10.1086/317969)
- Haywood, R. D., Collier Cameron, A., Queloz, D., et al. 2014, *MNRAS*, 443, 2517, doi: [10.1093/mnras/stu1320](https://doi.org/10.1093/mnras/stu1320)
- Hinkel, N. R., Timmes, F. X., Young, P. A., Pagano, M. D., & Turnbull, M. C. 2014, *AJ*, 148, 54, doi: [10.1088/0004-6256/148/3/54](https://doi.org/10.1088/0004-6256/148/3/54)

- Hodapp, K. W., Jensen, J. B., Irwin, E. M., et al. 2003, *PASP*, 115, 1388, doi: [10.1086/379669](https://doi.org/10.1086/379669)
- Howard, A. W., & Fulton, B. J. 2016, *PASP*, 128, 114401, doi: [10.1088/1538-3873/128/969/114401](https://doi.org/10.1088/1538-3873/128/969/114401)
- Howard, A. W., Johnson, J. A., Marcy, G. W., et al. 2010, *ApJ*, 721, 1467, doi: [10.1088/0004-637X/721/2/1467](https://doi.org/10.1088/0004-637X/721/2/1467)
- Howard, A. W., Marcy, G. W., Bryson, S. T., et al. 2012, *ApJS*, 201, 15, doi: [10.1088/0067-0049/201/2/15](https://doi.org/10.1088/0067-0049/201/2/15)
- Howell, S. B., Everett, M. E., Sherry, W., Horch, E., & Ciardi, D. R. 2011, *The Astronomical Journal*, 142, 19, doi: [10.1088/0004-6256/142/1/19](https://doi.org/10.1088/0004-6256/142/1/19)
- Huber, D., Zinn, J., Bojsen-Hansen, M., et al. 2017, *ApJ*, 844, 102, doi: [10.3847/1538-4357/aa75ca](https://doi.org/10.3847/1538-4357/aa75ca)
- Isaacson, H., & Fischer, D. 2010, *The Astrophysical Journal*, 725, 875, doi: [10.1088/0004-637X/725/1/875](https://doi.org/10.1088/0004-637X/725/1/875)
- Jenkins, J. M., Twicken, J. D., McCauliff, S., et al. 2016, in *Proc. SPIE*, Vol. 9913, Software and Cyberinfrastructure for Astronomy IV, 99133E, doi: [10.1117/12.2233418](https://doi.org/10.1117/12.2233418)
- Jensen, E. 2013, Tapir: A web interface for transit/eclipse observability, *Astrophysics Source Code Library*. <http://ascl.net/1306.007>
- Kempton, E. M. R., Bean, J. L., Louie, D. R., et al. 2018, *PASP*, 130, 114401, doi: [10.1088/1538-3873/aad6f6](https://doi.org/10.1088/1538-3873/aad6f6)
- Kipping, D. M. 2013, *MNRAS*, 435, 2152, doi: [10.1093/mnras/stt1435](https://doi.org/10.1093/mnras/stt1435)
- Kreidberg, L., Koll, D. D. B., Morley, C., et al. 2019, *Nature*, 573, 87, doi: [10.1038/s41586-019-1497-4](https://doi.org/10.1038/s41586-019-1497-4)
- Li, G., Dai, F., & Becker, J. 2020, *ApJL*, 890, L31, doi: [10.3847/2041-8213/ab72f4](https://doi.org/10.3847/2041-8213/ab72f4)
- Li, J., Tenenbaum, P., Twicken, J. D., et al. 2019, *PASP*, 131, 024506, doi: [10.1088/1538-3873/aaf44d](https://doi.org/10.1088/1538-3873/aaf44d)
- Lindgren, L., Hernández, J., Bombrun, A., et al. 2018, *A&A*, 616, A2, doi: [10.1051/0004-6361/201832727](https://doi.org/10.1051/0004-6361/201832727)
- Lithwick, Y., Xie, J., & Wu, Y. 2012, *ApJ*, 761, 122, doi: [10.1088/0004-637X/761/2/122](https://doi.org/10.1088/0004-637X/761/2/122)
- Lopez, E. D., & Fortney, J. J. 2014, *ApJ*, 792, 1, doi: [10.1088/0004-637X/792/1/1](https://doi.org/10.1088/0004-637X/792/1/1)
- Lund, M. L. e. a. 2020, submitted
- Marcy, G. W., & Butler, R. P. 1992, *PASP*, 104, 270, doi: [10.1086/132989](https://doi.org/10.1086/132989)
- McCully, C., Volgenau, N. H., Harbeck, D.-R., et al. 2018, in *Society of Photo-Optical Instrumentation Engineers (SPIE) Conference Series*, Vol. 10707, Proc. SPIE, 107070K, doi: [10.1117/12.2314340](https://doi.org/10.1117/12.2314340)
- Mills, S. M., Howard, A. W., Petigura, E. A., et al. 2019, *AJ*, 157, 198, doi: [10.3847/1538-3881/ab1009](https://doi.org/10.3847/1538-3881/ab1009)
- Narita, N., Fukui, A., Kusakabe, N., et al. 2019, *J. Astron. Telesc. Instruments, Syst.*, 5, 015001, doi: [10.1117/1.JATIS.5.1.015001](https://doi.org/10.1117/1.JATIS.5.1.015001)
- Parviainen, H., Palle, E., Zapatero-Osorio, M. R., et al. 2020, *A&A*, 633, A28, doi: [10.1051/0004-6361/201935958](https://doi.org/10.1051/0004-6361/201935958)
- Petigura, E. A. 2015, PhD thesis, University of California, Berkeley
- Petigura, E. A., Howard, A. W., & Marcy, G. W. 2013, *Proceedings of the National Academy of Sciences*, 110, 19273, doi: [10.1073/pnas.1319909110](https://doi.org/10.1073/pnas.1319909110)
- Petrovich, C., Deibert, E., & Wu, Y. 2019, *AJ*, 157, 180, doi: [10.3847/1538-3881/ab0e0a](https://doi.org/10.3847/1538-3881/ab0e0a)
- Piskunov, N., & Valenti, J. A. 2017, *Astronomy and Astrophysics*, 597, A16
- Pu, B., & Lai, D. 2019, *MNRAS*, 488, 3568, doi: [10.1093/mnras/stz1817](https://doi.org/10.1093/mnras/stz1817)
- Rajpaul, V., Buchhave, L. A., & Aigrain, S. 2017, *MNRAS*, 471, L125, doi: [10.1093/mnrasl/slx116](https://doi.org/10.1093/mnrasl/slx116)
- Rappaport, S., Sanchis-Ojeda, R., Rogers, L. A., Levine, A., & Winn, J. N. 2013, *ApJL*, 773, L15, doi: [10.1088/2041-8205/773/1/L15](https://doi.org/10.1088/2041-8205/773/1/L15)
- Ricker, G. R., Winn, J. N., Vanderspek, R., et al. 2015, *Journal of Astronomical Telescopes, Instruments, and Systems*, 1, 014003, doi: [10.1117/1.JATIS.1.1.014003](https://doi.org/10.1117/1.JATIS.1.1.014003)
- Rodriguez, D. 2016, Dr-Rodriguez/Kinematics-App: Stellar Kinematics V1.0, v1.0, Zenodo, doi: [10.5281/zenodo.192159](https://doi.org/10.5281/zenodo.192159)
- Rogers, L. a. 2015, *ApJ*, 801, 41, doi: [10.1088/0004-637X/801/1/41](https://doi.org/10.1088/0004-637X/801/1/41)
- Salaris, M., Chieffi, A., & Straniero, O. 1993, *ApJ*, 414, 580, doi: [10.1086/173105](https://doi.org/10.1086/173105)
- Sanchis-Ojeda, R., Rappaport, S., Winn, J. N., et al. 2014, *ApJ*, 787, 47, doi: [10.1088/0004-637X/787/1/47](https://doi.org/10.1088/0004-637X/787/1/47)
- Sanchis-Ojeda, R., Winn, J. N., Dai, F., et al. 2015, *ApJL*, 812, L11, doi: [10.1088/2041-8205/812/1/L11](https://doi.org/10.1088/2041-8205/812/1/L11)
- Schönrich, R., & Binney, J. 2009a, *MNRAS*, 399, 1145, doi: [10.1111/j.1365-2966.2009.15365.x](https://doi.org/10.1111/j.1365-2966.2009.15365.x)
- . 2009b, *MNRAS*, 396, 203, doi: [10.1111/j.1365-2966.2009.14750.x](https://doi.org/10.1111/j.1365-2966.2009.14750.x)
- Sharma, S., Stello, D., Buder, S., et al. 2018, *MNRAS*, 473, 2004, doi: [10.1093/mnras/stx2582](https://doi.org/10.1093/mnras/stx2582)
- Silva Aguirre, V., Bojsen-Hansen, M., Slumstrup, D., et al. 2018, *MNRAS*, 475, 5487, doi: [10.1093/mnras/sty150](https://doi.org/10.1093/mnras/sty150)
- Smith, J. C., Stumpe, M. C., Van Cleve, J. E., et al. 2012, *PASP*, 124, 1000, doi: [10.1086/667697](https://doi.org/10.1086/667697)
- Stassun, K. G., Collins, K. A., & Gaudi, B. S. 2017, *AJ*, 153, 136, doi: [10.3847/1538-3881/aa5df3](https://doi.org/10.3847/1538-3881/aa5df3)
- Stassun, K. G., & Torres, G. 2018, *ApJ*, 862, 61, doi: [10.3847/1538-4357/aaca6c](https://doi.org/10.3847/1538-4357/aaca6c)
- Stassun, K. G., Oelkers, R. J., Pepper, J., et al. 2018, *AJ*, 156, 102, doi: [10.3847/1538-3881/aad050](https://doi.org/10.3847/1538-3881/aad050)
- Stumpe, M. C., Smith, J. C., Catanzarite, J. H., et al. 2014, *PASP*, 126, 100, doi: [10.1086/674989](https://doi.org/10.1086/674989)

- Stumpe, M. C., Smith, J. C., Van Cleve, J. E., et al. 2012, *PASP*, 124, 985, doi: [10.1086/667698](https://doi.org/10.1086/667698)
- Tamayo, D., Cranmer, M., Hadden, S., et al. 2020, *Proceedings of the National Academy of Sciences*, 117, 18194, doi: [10.1073/pnas.2001258117](https://doi.org/10.1073/pnas.2001258117)
- Ting, Y.-S., Conroy, C., Rix, H.-W., & Asplund, M. 2018, *The Astrophysical Journal*, 860, 159
- Tokovinin, A., Mason, B. D., Hartkopf, W. I., Mendez, R. A., & Horch, E. P. 2018, *AJ*, 155, 235, doi: [10.3847/1538-3881/aabf8d](https://doi.org/10.3847/1538-3881/aabf8d)
- Twicken, J. D., Catanzarite, J. H., Clarke, B. D., et al. 2018, *PASP*, 130, 064502, doi: [10.1088/1538-3873/aab694](https://doi.org/10.1088/1538-3873/aab694)
- Valenti, J. A., & Piskunov, N. 1996, *Astronomy and Astrophysics Supplement*, 118, 595
- Van Eylen, V., Albrecht, S., Huang, X., et al. 2019, *AJ*, 157, 61, doi: [10.3847/1538-3881/aaf22f](https://doi.org/10.3847/1538-3881/aaf22f)
- van Saders, J. L., Ceillier, T., Metcalfe, T. S., et al. 2016, *Nature*, 529, 181, doi: [10.1038/nature16168](https://doi.org/10.1038/nature16168)
- van Saders, J. L., & Pinsonneault, M. H. 2013, *ApJ*, 776, 67, doi: [10.1088/0004-637X/776/2/67](https://doi.org/10.1088/0004-637X/776/2/67)
- Weiss, L. M., & Marcy, G. W. 2014, *ApJ*, 783, L6, doi: [10.1088/2041-8205/783/1/L6](https://doi.org/10.1088/2041-8205/783/1/L6)
- Weiss, L. M., Rogers, L. A., Isaacson, H. T., et al. 2016, *ApJ*, 819, 83, doi: [10.3847/0004-637X/819/1/83](https://doi.org/10.3847/0004-637X/819/1/83)
- Yee, S. W., Petigura, E. A., & von Braun, K. 2017, *ApJ*, 836, 77, doi: [10.3847/1538-4357/836/1/77](https://doi.org/10.3847/1538-4357/836/1/77)
- Ziegler, C., Tokovinin, A., Briceño, C., et al. 2020, *AJ*, 159, 19, doi: [10.3847/1538-3881/ab55e9](https://doi.org/10.3847/1538-3881/ab55e9)